A Numerical Analysis of the Dynamic Stall Mechanisms on a Helicopter Rotor From Light to Deep Stall

Camille Castells, François Richez, Michel Costes

A Numerical Analysis of the Dynamic Stall Mechanisms on a Helicopter Rotor From Light to Deep Stall

Camille Castells*

PhD Student

ONERA, The French Aerospace Lab, Meudon, France

François Richez

Research Scientist

ONERA, The French Aerospace Lab, Meudon, France

Michel Costes

Research Scientist

ONERA, The French Aerospace Lab, Meudon, France

Abstract

A loose coupling methodology between Computational Fluid Dynamics and Comprehensive Analysis codes (*elsA*/HOST) is used to simulate a helicopter rotor in dynamic stall condition. Three stalled forward flight conditions have been selected in the wind tunnel 7A rotor test data to investigate the evolution of the stall mechanisms from a light stall to a deep stall condition. A decrease in the RPM is used to increase the rotor load. The lower the RPM, the more severe the stall is. A double stall is observed in the lowest RPM case. The simulations are in satisfactory agreement with the experiment and are used to identify the mechanisms leading to the different stall events, notably the blade-vortex

*Corresponding author; email:castells.camille@onera.fr

Presented at the Vertical Flight Society 75th Annual Forum & Technology Display, Philadelphia, Pennsylvania, May 13 - 16, 2019.

interaction. Rotormaps of the flow-separation regions are computed from numerical results and similar regions of separated flow are observed in all the cases. These flow-separations originate from different aeroelastic mechanisms depending on their position on the rotor disk. As the rotor thrust coefficient is increased, some of these flow-separations grow and lead to stall events.

Nomenclature

R	Rotor radius, m
c	Blade chord, m
Ω	Rotational speed, rpm
M_{tip}	Tip Mach number
μ	Advance ratio
σ	Rotor solidity
C_L/σ	Rotor lift coefficient
C_X/σ	Rotor propulsive force coefficient
M^2C_n	Section normal force coefficient
M^2C_m	Section pitching moment coefficient
α_t	Shaft angle, deg
θ_0	Collective pitch angle, deg
θ_{1c}	Lateral cyclic pitch angle, deg
θ_{1s}	Longitudinal cyclic pitch angle, deg
β	Flap angle, deg
β_{1c}	Longitudinal flapping angle, deg
β_{1s}	Lateral flapping angle, deg
ψ	Blade azimuthal position, deg
K_p	Pressure coefficient
$K_{p,crit}$	Critical pressure coefficient where the local Mach number equals one
x_{sep}/c	Chordwise position of flow-separation point

l_{sep}/c	Chordwise length of flow-separation region
$\vec{U_e}$	Velocity vector at the edge of the boundary layer
$\vec{U_\tau}$	Skin friction vector
V_∞	Freestream velocity, m/s
V_{iz}	Vertical component of the induced velocity, m/s
α_i	Induced angle of attack, deg

Introduction

Dynamic stall is one of the most limiting phenomena occurring during helicopter operation, especially in forward flights or in maneuvers. In forward flight conditions, a dissymetry of airspeed is observed on the rotor disk with respect to the azimuthal position of the blade, due to the combination of rotating and advancing speeds. To balance the rotor loads and remove the corresponding rolling motion, the angle of attack has to be periodically modified. It is reduced on the advancing blade side and increased on the retreating blade side where the airspeed is lower. For high thrust flight conditions, the local angle of attack on the retreating blade sections exceeds the static stall angle and reaches a critical angle of attack. Beyond this angle, the boundary layer massively separates, the lift is considerably decreased and a strong negative pitching moment is observed. This phenomenon, called dynamic stall, occurring at each rotor revolution, causes vibrations and eventually can jeopardize the blade structure (Ref. 1).

Dynamic stall remains a challenging phenomenon of the rotorcraft environment for numerical prediction since it involves several mechanisms which are not well understood and require accurate numerical methods. One can name three-dimensional unsteady separated flow, transonic flow including shocks, reverse flow, blade-vortex interaction, vortex shedding or fluid-structure coupling.

A renewed interest on the problem could be noted over the last twenty years thanks to the progress of Computational Fluid Dynamics (CFD) in dealing with viscous separated flows, progressively switching from simplified cases to more realistic ones.

Until very recently, most studies dedicated to dynamic stall were carried out on simplified config-

urations, typically two-dimensional airfoils in oscillating pitching motion simulating the evolution of the angle of attack during a rotor revolution (Ref. 2). Several experimental investigations such as Refs. 3–6 and numerical studies as Refs. 7, 8 allowed scientists to investigate and obtain a better understanding of the different mechanisms occurring during a dynamic stall event on airfoils. They highlighted the hysteresis aspect of the lift and the pitching moment. They also brought out that the sharp decrease in pitching moment is observed before the decrease in lift. It is explained by the shedding of the dynamic stall vortex travelling downstream from leading edge to trailing edge. Two-dimensional Unsteady Reynolds-Averaged Navier-Stokes (URANS) simulations allowed the determination of the numerical requirements needed to capture dynamic stall events for a reduced time-cost. Among these numerical investigations, one can mention the work of Refs. 8, 9 on the time and space resolution, the work of Srinivasan *et al.* in Ref. 10 on turbulence modelling or the investigations carried out on the influence of the prediction of boundary layer transition on stall in Refs. 8, 11, 12. In Ref. 13, Costes *et al.* also highlighted that two-dimensional numerical simulations cause an earlier onset of the stall event, overpredict the separation and delay the reattachment with respect to similar three-dimensional configurations.

It was shown experimentally in three-dimensional studies on oscillating airfoil in Ref. 14 that the dynamic stall is a three-dimensional process. It starts at a very localized position and then seems to spread spanwise. Then, three-dimensional configurations were also investigated to take into account the influence of the finite span character of the blade and the impact of the tip vortex on stall onset. In Ref. 15, Le Pape *et al.* showed experimentally on an OA209 wing that three-dimensional mechanisms are present during a stall event. The tip vortex of the wing induces a downward flow which tends to delay the stall onset in the blade-tip region. Some numerical studies, as Refs. 16–19 used experimental data to validate the URANS simulations and to provide the numerical requirements and the physical models adapted for stall prediction in three-dimensional configurations.

The next step in the dynamic stall studies is the inclusion of the blade rotation. Rotating blades in pitching oscillation motion have been investigated using experiments as in Refs. 20, 21 and then using numerical simulations such as Refs. 22–24. The effect of rotation is to keep the stall vortex closer to the blade surface with respect to a non-rotating configuration.

In a realistic rotor environment, the dynamic stall mechanisms are expected to be quite different from the isolated wing since blade-wake interaction or blade articulation and deformation can influence the stall onset by modifying locally the angle of attack. In Ref. 25, Bousman was one of the first to investigate the dynamic stall in a complete rotor environment on three conditions extracted from flight tests of the UH-60A Black Hawk helicopter (Ref. 26), namely two maneuvers and one stalled forward flight. More recently, dynamic stall has been investigated using wind tunnel experiments on a fully equipped helicopter model in Ref. 27. It showed that the flow is highly three-dimensional and complex due to combined effects of the blade motion and other unsteady aerodynamic phenomena, such as the blade-vortex interaction occurring in the same region of the blade as the dynamic stall. In Ref. 28, Potsdam *et al.* developed a fluid/structure coupling strategy between a Comprehensive Analysis (CA) code and a CFD solver. Three flight conditions from Ref. 26 including the stalled forward flight studied by Bousman were computed. The coupling computations gave a good agreement with respect to the experimental data available. Yeo *et al.* in Ref. 29 and Ortun *et al.* in Ref. 30 also validated CFD/CA coupled simulations on 7A rotor configurations. In Ref. 31, Richez *et al.* provided the numerical requirements necessary to predict stall at high thrust in forward flight. Recent works, as Refs. 30–34, on different stalled flight conditions, including turn flight in Ref. 34, highlighted the capability of numerical tools to predict dynamic stall on rotor configurations, especially in forward flight. They provide some clues on the several mechanisms involved in the stall onset such as blade-vortex interaction in a high angle of attack area as Refs. 33, 35 or the torsional response of the blade in Ref. 35.

Promising results of the CFD/CA coupling process to investigate the dynamic stall phenomenon have been presented but they mostly used one single flight condition. The objective of the present work is to get a better understanding of the mechanisms occurring during stall events in a rotor environment, especially from a light to a deep stall case. Three forward flight conditions with potentially different stall mechanisms are compared using coupled CFD/CA simulations. One of the cases is the one investigated by Richez in Refs. 31, 35. However, the computations are performed with a smaller time step and the investigation of the flow separation region is based on a new criterion leading to improved rotormaps of the separated flow on the rotor disk.

Experimental Database

A wide range of flight conditions of the model-scale 7A rotor, represented in Figure 1, have been tested in the transonic closed circuit S1MA wind tunnel at ONERA Modane test center, France, in 1991 (Ref. 36). The 7A rotor, of radius R=2.1 m, is composed of four articulated blades of constant chord c = 0.14 m and constant aerodynamic twist rate of -8.3 deg/R. The blade is made of two airfoils. The 13% relative thickness OA213 airfoil is used from inboard to 0.75R and the 9% relative thickness OA209; from 90% of the rotor radius to the tip. A linear interpolation of the airfoil shape between OA213 and OA209 is used to define the blade geometry for radius from 0.75R to 0.90R. An extensive database is available including high thrust and high speed cases. It provides unsteady pressure measurements, integrated section normal forces and pitching moments at the five blade radial stations r/R = 0.5, 0.7, 0.825, 0.915, and 0.975 as well as blade bending moments, torsion moments and motion (rigid angles and elastic deformations) at sections r/R = 0.3, 0.4, 0.55, 0.65, 0.75 and 0.85.

Three configurations have been selected from the database for the numerical investigation presented in this work. They reflect the influence of the rotor load on the dynamic stall mechanisms by modifying the rotor rotational speed (defined in revolutions per minute: RPM). All selected conditions have the same propulsive and lift forces. Table 1 summarizes the flow parameters for each flight condition investigated. The moderate RPM case in the present work corresponds to the flight condition investigated in Ref. 35.

To maintain the same thrust, an increase of the angle of attack is necessary when the RPM is decreased. An increase of the pitch angle θ and of the flapping amplitude is actually obtained (Table 1). It results in an amplification of the stall event when the RPM is decreased.

The objective of the present work is to get an understanding of the mechanisms occurring during light, moderate and deep stall flight conditions by using numerical simulations.

Computational Methodology

This work uses a loose coupling strategy between CFD and CA, similarly to the method presented by Potsdam in Ref. 28.

The CFD part of the coupling procedure is performed with the URANS finite volume *elsA* solver developed by ONERA (Ref. 37). A Chimera approach is done using the pre- and post-processing tool Cassiopee (Ref. 38), with near body curvilinear structured grids around the blades and around the experimental test stand, and background Cartesian grids (Figure 2). The blade near body grid is composed of $\mathbf{5.7 \times 10^6}$ points (Table 3). The k-ω Kok (Ref. 39) SST turbulence model is used because it has shown a good capability to predict dynamic stall events in previous works (Refs. 32,35). The time derivative is discretized with a second order implicit Gear scheme. At each time step, the non-linear problem is solved by an iterative Newton process. The time step is set to $\boldsymbol{\Delta\psi} = 0.225$ deg with 30 sub-iterations in the Newton iterative process in order to get second-order time-accurracy (Ref. 40). Preliminary works consisted in evaluating the time step required to capture the dynamic stall phenomenon on the MRPM case (not shown). The time step used in the following analysis gives a solution which is weakly dependent on the time resolution during the stall event, as the airloads do not significantly vary when the time step is reduced below $\boldsymbol{\Delta\psi} = 0.225$ deg. Thus, although this flight condition is the one investigated by Richez in Ref. 35, the present computation is identical to those of Refs. 35,41 apart from the time step which was reduced from $\boldsymbol{\Delta\psi} = 0.3$ deg to $\boldsymbol{\Delta\psi} = 0.225$ deg.

The HOST comprehensive analysis code developed by Airbus Helicopters (Ref. 42) is used to take into account the blade motion and deformation in the coupled simulations. It is based on the lifting line theory for aerodynamics and beam theory with modal decomposition to describe the blade structure. Seven modes and seven harmonics have been used to characterize the blade deformation. The aerodynamic loads from the URANS computations are used by the comprehensive code to compute the trim control angles and also the kinematics and deformations of the blades, which are, then, used by *elsA* to prescribe the motion and deformation of the blade grids. The coupling between the

codes is made after each rotor revolution. For each flight condition, as done in the experiments, we performed a four degree-of-freedom trim law. The shaft angle α_t and the collective and cyclic pitch angles (respectively θ_0, θ_{1c} and θ_{1s}) are used as trim variables. The targets are the rotor thrust C_L/σ and the rotor propulsive force C_X/σ completed with the so-called Modane flapping law which imposes $\beta_{1s} = 0$ and $\beta_{1c} + \theta_{1s} = 0$. The simulations are stopped when the trim targets (Table 2) are reached; and when the control angles and the airloads do not vary anymore between consecutive iterations of the coupling process. For the present computations, such a convergence typically requires 5 to 10 revolutions as illustrated in Figure 3 for the deep stall case investigated in this study. The deeper the stall is, the longer the convergence takes to be reached.

Validation

The converged trim control angles obtained by the coupling process are compared to the experimental data available for each flight condition. The numerical calculations are in good agreement with the wind tunnel results as shown in Table 4.

The trim angles are well estimated by the coupling method with a difference of less than 0.3 deg from the experiment for all control angles. The test-stand used during the experiment has been taken into account in the computations (Figure 2) since Ortun *et al.* in Ref. 30 shows that it improves the lateral cyclic pitch angle estimation of the simulation by deflecting the flow toward the rotor disk. The test-stand creates an upwash flow on the front of the rotor, $\psi = 180\,\mathrm{deg}$, and a downwash flow on the rear part, $\psi = 0\,\mathrm{deg}$, thus inducing a decrease of the local angle of attack at $\psi = 0\,\mathrm{deg}$ and an increase at $\psi = 180\,\mathrm{deg}$, which is directly balanced by the lateral pitch angle, as discussed in Ref. 35.

The experimental sectional normal force and pitching moment coefficients M^2C_n and M^2C_m are compared to the computed results in Figures 4 to 9. Only the cycle-to-cycle averaged experimental data are available and used for comparison with URANS simulations. Furthermore, in order to avoid a systematic error to get these quantities from *elsA*, the same integration procedure applied in the tests was used by integrating the computed pressure at the location of the unsteady pressure

transducers.

For the moderate RPM test case, the dynamic stall event, which is characterized by a severe loss of lift and a sharp negative pitching moment on the retreating blade ($\mathbf{180\,deg} \leq \psi \leq \mathbf{360\,deg}$) is captured by the simulation. The decrease of $\boldsymbol{M^2C_n}$ and $\boldsymbol{M^2C_m}$ is well predicted by the coupled calculations (Figures 4 and 5). The minimum of $\boldsymbol{M^2C_n}$, obtained at $\psi = \mathbf{300\,deg}$ for the $\boldsymbol{r/R} = \mathbf{0.915}$ section, is slightly overestimated but, in general, the normal force coefficient during the stall event is almost perfectly predicted in amplitude and in phase for all the other sections shown in Figure 4. The pitching moment coefficient is more sensitive and more difficult to capture, but the agreement between simulation and experiment is satisfactory since the moment stall occurs at the right azimuthal position and with a comparable peak-to-peak variation. The minimum of $\boldsymbol{M^2C_m}$ is reached at $\psi = \mathbf{290\,deg}$ for the $\boldsymbol{r/R} = \mathbf{0.915}$ section. One can notice, in Figure 5, that the minimum value reached is underestimated (more negative) by the CFD/CA computation. A second small variation of $\boldsymbol{M^2C_m}$, which is visible but less intense in the experimental data, is predicted by the simulation for $\boldsymbol{r/R} = \mathbf{0.915}$ and for $\boldsymbol{r/R} = \mathbf{0.975}$, $\mathbf{320\,deg} \leq \psi \leq \mathbf{330\,deg}$.

For the high RPM case, the stall is weaker than the one observed in the MRPM case. Figure 6 shows that the sectional normal force coefficients are well captured by the calculation for all the sections and that the loss of lift is less intense and less sudden than the one observed in the MRPM case. Only one section ($\boldsymbol{r/R} = \mathbf{0.915}$) undergoes a steep decrease of $\boldsymbol{M^2C_m}$ characteristic of a stall event, as shown in the experimental data in Figure 7. However, one can notice, in Figure 7, that the negative pitching moment peak characteristic of stall is almost missed by the simulation. A slight decrease in the pitching moment is indeed observed at stall position $\psi = \mathbf{290\,deg}$ for $\boldsymbol{r/R} = \mathbf{0.915}$ but it is strongly underestimated with respect to the experimental data. This kind of behaviour has already been observed in two-dimensional configurations. Light stalls where the pitch angle oscillations remain close to the stall angle are more difficult to capture by numerical simulations.

To maintain the same thrust, the reduction of RPM leads to an increase of the angle of attack and to an earlier stall onset. For the highest rotational speed (HRPM), stall appears at the $\boldsymbol{r/R} = \mathbf{0.915}$ section only at an azimuthal position of 280 $\mathbf{deg}$, while it starts at 250 $\mathbf{deg}$ for the lowest RPM

tested (LRPM). One can also notice that for the most critical case (LRPM), a second strong stall event occurs at 330 $\mathbf{deg}$ for the $\boldsymbol{r/R = 0.915}$ section, which is not seen in the other cases. The two dynamic stall events observed for the lower RPM are captured by the computations in good agreement with experimental results (Figures 8 and 9). Both of the events are however overestimated (more severe) in terms of pitching moment coefficient peak-to-peak variations but are well captured in terms of azimuthal phase of the stall onset, the first stall event starting at $\boldsymbol{\psi = 250\,deg}$ and the second one at $\mathbf{330\,deg}$ at the section $\boldsymbol{r/R = 0.915}$ (Figure 9).

The stall induces a strong pitching moment variation that induces a torsion moment variation that is transmitted to the pitch-link loads. Thus, the prediction of the structural loads has to be validated. The coupled procedure shows a good capability to predict the structural loads of the rotor blades. Figure 10 depicts the evolution of the torsional moments obtained by the CA/CFD with respect to the experiment. Two sections ($\boldsymbol{r/R = 0.3}$ and $\boldsymbol{r/R = 0.65}$) of the blade are represented. The computations are in good agreement with the experiments. The 5/rev frequency content of the torsional moment is well predicted by the *elsA*/HOST computations for all cases. The amplitudes are overestimated in the MRPM and the LRPM cases but the azimuthal phase correlation between the simulation and the experimental data is satisfactory in both sections (Figures 10 *b)*, *c)*, *e)* and *f)*). For the HRPM case, the amplitude is slightly underestimated, probably because of the underestimation of the pitching moment peak at the blade-tip observed in Figure 7 ($\boldsymbol{r/R = 0.915}$).

It can be concluded that the loose coupling method correctly captures dynamic stall events for these three different flight conditions. Therefore, the numerical results will be used to identify the stall regions and their features during these flight conditions in the next section.

Analysis

Description of the separated flow regions

In this section, a post-processing tool that provides the features of the flow-separation regions over the rotor disk based on the results of the CFD simulation is proposed. The objective is to quantify the evolution of the flow-separations as the RPM is reduced. Thus, rotormaps of the chordwise flow-

separation point position x_{sep}/c and chordwise flow-separation length $l_{sep/c}$ at each radial section and azimuthal step have been established and are used to identify the flow-separation regions and their length in each flight condition. In Ref. 35, Richez proposed a criterion based on the shape factor to identify the flow-separation regions on the rotor disk and to compute rotormaps of these areas of separated flow. However, this criterion is not able to clearly detect the reattachment and thus the flow-separation length in these flow conditions. A criterion based on the friction lines and the velocity vector is here prefered to get all the flow-separation features. The separation point, x_{sep}, is defined as the point where the dot product between the friction vector and the velocity at the edge of the boundary layer (boundary layer thickness based on vorticity and shear stress, Ref. 43) becomes negative and, in the same way, the reattachment point is reached when it becomes positive again as shown in Figure 11. The leading edge (LE) is the origin of the local chordwise axis so that $x/c = 0$ represents the leading edge position while $x/c = 1$ is the trailing edge (TE). Thus, $x_{sep}/c = 0$ defines a flow-separation at the very leading edge while $x_{sep}/c = 1$ means that there is no flow-separation. In the same way, the chordwise length l_{sep} of the flow-separation at each radial and azimuthal position is computed and $l_{sep}/c = 0$ means that no flow-separation is detected while $l_{sep}/c \approx 1$ defines a fully separated flow along the chord.

The rotormaps of the chordwise flow-separation point position computed for the three flight conditions are presented in Figure 12 and rotormaps of the chordwise flow-separation length is illustrated in Figure 13. They reveal four flow-separation regions for all cases. For the sake of clarity, only the frontmost flow-separation is illustrated and no case of two prominent flow-separations occuring at the same section has been observed. These regions are named after their position on the rotor disk ("A", "B", "C" and "D") in Figure 12. They also exhibit an increase in the global separated flow area on the rotor disk as the RPM is decreased, while maintaining the same thrust. Furthermore, more flow-separation regions are illustrated by the rotormap of the flow-separation point position in Figure 12 for the MRPM case compared to the one computed by Richez in Ref. 35. In Ref. 35, data were filtered to avoid uncertainties related to the shape factor in separated flows. Consequently, some flow-separation regions are not detected in Ref. 35. The criterion used in this study is more efficient to identify and characterize the flow-separation regions than the one used by Richez in Ref. 35.

The first flow-separation occurring on the blade is located on the inner part of the blade ($\mathbf{0.4} \leq r/R \leq \mathbf{0.8}$) in the third quadrant of the rotor disk, $\mathbf{180\,deg} \leq \psi \leq \mathbf{270\,deg}$ of every cases considered. This region is referred to as "A" in Figure 12 and is characterized by a trailing edge separation. The boundary layer separates at the trailing edge at $r/R = \mathbf{0.6}$, for $\mathbf{165\,deg} \leq \psi \leq \mathbf{180\,deg}$, depending on the case, and moves towards the leading edge when the blade pursues its revolution. Figure 12 also highlights that the flow-separation moves further upstream when the RPM is decreased. Thus, the flow-separation point does not reach further than the quarter chord in the high RPM case, $x_{sep}/c = \mathbf{0.3}$ at $r/R = \mathbf{0.5}$ and $\psi = \mathbf{250\,deg}$. In contrast, it reaches the leading edge, $x_{sep}/c \approx \mathbf{0}$, for the two lower RPM cases and at an increasingly early azimuthal position of the blade. For the $r/R = \mathbf{0.5}$ section, the separation point reaches the leading edge at $\psi = \mathbf{240\,deg}$ for the moderate RPM case and at $\psi = \mathbf{225\,deg}$ for the lowest RPM case. It induces the airload variations observed in Figures 4 *a)*, 5 *a)*, 8 *a)* and 9 *a)*. The separation also spreads radially, contaminating more outboard sections of the blade. Figure 13 shows that, for the two lowest RPM cases, this region leads to a massive flow-separation ($l_{sep}/c \geq \mathbf{0.9}$) since it reaches the leading edge. This topology of flow-separation is refered to as "trailing edge stall" in the literature and is responsible for the M^2C_n and M^2C_m variations observed in Figures 4, 5, 8 and 9, at $r/R = \mathbf{0.5}$, while no stall is observed in the HRPM case in this section, Figures 8 and 9.

A second flow-separation region occurs near the blade-tip for $\mathbf{210\,deg} \leq \psi \leq \mathbf{310\,deg}$ in all cases and is referred to as "B" in Figure 12. Firstly, for $\psi \leq \mathbf{270\,deg}$, the separation suddenly appears at the leading edge of the blade and immediately reattaches as illustrated in Figure 13, the flow-separation length being less than $\mathbf{5\%}$ of the blade chord. However, as the blade reaches a critical azimuthal position, the separation bubble bursts for the two lowest RPM cases. Figure 13 exhibits massive flow-separations ($l_{sep}/c = \mathbf{1}$) leading to the stall events seen on these two cases near the blade-tip at $r/R = \mathbf{0.915}$ and $r/R = \mathbf{0.975}$ in Figures 4 to 9. According to the M^2C_m plot, dynamic stall occurs at $\psi = \mathbf{290\,deg}$ in the MRPM case and at $\psi = \mathbf{270\,deg}$ in the LRPM case. The separation bubble does not burst in the high RPM case since the flow-separation remains smaller than $\mathbf{10\%}$ of the blade chord. However, it can be expected that the flow-separation length is underestimated by the simulation in this case since the slight moment stall is missed in Figure 7.

The next flow-separation area, referred to as "C", is located at the end of the fourth quadrant ($\mathbf{320\,deg} \leq \psi \leq \mathbf{10\,deg}$) also at the blade-tip region (Figure 12). For all the cases, the boundary layer first separates and immediately reattaches leading to a small separation bubble. As the azimuth increases, the bubble expands and evolves into a massive flow-separation only for the LRPM test case. This flow-separation leads to the second stall event observed for the airloads in Figures 8 and 9. For the moderate RPM case, the separated flow reaches 30% of the blade chord which can explain the small pitching moment fluctuations seen in Figure 5 at $\boldsymbol{r/R > 0.915}$ and $\mathbf{320\,deg} \leq \psi \leq \mathbf{330\,deg}$. For the HRPM case, the separation bubble of region "C" (Figure 12) does not reach a length sufficient to influence the loads since $\boldsymbol{l_{sep}/c < 5\%}$ (Figure 13).

The flow-separation region "D" (Figure 12) appears on the advancing side ($\mathbf{0\,deg} \leq \psi \leq \mathbf{90\,deg}$) in the tip region of the blade. The flow separates at the leading edge but the separation bubble does not reach a size ($\boldsymbol{l_{sep}}$) that leads to stall. For all cases, Figure 13 shows that $\boldsymbol{l_{sep}/c < 10\%}$ in region "D". In the LRPM case, the region "D" is composed of two different lobes connected to each other by a thin separated flow region (Figure 12). The first lobe is located around $\boldsymbol{\psi = 30\,deg}$, when the other one is around $\boldsymbol{\psi = 90\,deg}$.

The characteristics of these different flow-separation regions and their mechanisms are explained in more detail in the next section.

Analysis of Flow-Separation in Region "A"

In Ref. 35, Richez highlighted that the blade-vortex interaction (BVI) seems to trigger the dynamic stall onset on realistic configurations of helicopter rotor. The flight condition investigated in Ref. 35 corresponds to the moderate RPM case considered in the present work.

Thus, the effect of the BVI on the stall event of region "A" is investigated for each flow condition. An analytical tool was implemented to estimate the location of the interaction between a blade and the tip vortex from the preceding blades. To do so, an analytical prediction of the position of the tip vortices emitted by the blades is first computed. A helicoidal shape of the vortex driven by the rotational velocity of the rotor and the translational speed of the aircraft is assumed. The lead-lag

and flap motions of the blade are considered in the computation as well as the shaft angle. The radial position of the interaction with the blade can then be easily determined as the intersection between the blade and the helicoidal vortex lines in the projection normal to the rotor disk. For clarification purposes, a snapshot of the analytical vortices for a blade at $\psi = 280\,\mathrm{deg}$ for the moderate RPM case is shown in Figure 14. The intersection point between the blade and the tip vortex path at the retreating blade is circled in black. A good agreement between the analytical vortex line and the vortex computed by the coupling simulation, represented by an isocontour of the Q-criterion, is observed which validates the analytical vortex position.

Finally, the radial position of this interaction is computed for each azimuth and shown with $\diamond$ symbols overlayed on the rotormaps of the chordwise flow-separation point (Figure 13) in Figure 15. For all cases, the flow-separation development follows the blade-vortex interaction line, especially in region "A".

The interaction occurring in region "A" starts at the tip of the blade at the azimuth $\psi = 90\,\mathrm{deg}$, when the blade is set at a low angle of incidence. Thus, the vortex passage does not induce a sufficient rise of angle of attack to trigger boundary layer separation. When the blade goes on with its revolution, the pitch angle is increased and the vortex influence becomes more critical. A flow-separation begins to develop from the trailing edge at $r/R = 0.6$ at the interaction point for $\psi \approx 180\,\mathrm{deg}$ and moves towards the leading edge as ψ and the angle of attack increase. The lower the RPM is, the earlier the stall occurs since the pitch angle is higher when the RPM is decreased.

The stall develops at the blade-vortex interaction point and then, as the azimuth and the angle of attack are increased, it spreads radially around the BVI position as illustrated in Figure 15.

Analysis of Flow-Separation in Region "B"

Figure 15 also shows that the region "B" is located in an area where the preceding blade-tip vortex is close to the blade. A small separation bubble at the leading edge is observed before the BVI, for $\psi < 270\,\mathrm{deg}$ for all cases in Figures 12 and 15, but this separation length remains smaller than 10% of the blade chord. When the tip vortex comes closer to the blade, it seems to trigger the bubble

bursting for the MRPM case. In this case, the sudden growth of the bubble size is occurring at the time of the interaction between the blade and the tip vortex ($\psi = \mathbf{280\,deg}$). However, for the LRPM case, the stall onset is occurring before the blade-vortex interaction. In Figure 16, an isocontour of the Q-criterion for a blade at the azimuthal position corresponding to the minimum of the $\boldsymbol{M^2C_m}$ in region "B" is represented for all the cases. At this position of the blade, the tip vortex is close to the blade-tip where the stall vortex is growing, especially in the two higher RPM cases. The dynamic stall vortex characterized by a high level of turbulent kinetic energy can be distinguished from tip vortices that are characterized by low level of turbulent kinetic energy. For the LRPM case, as observed in Figure 15, the stall occurs when the tip vortex is still far from the blade. At stall onset, the vortex is located $\mathbf{1}\boldsymbol{c}$ below the blade in the MRPM case while the vortex is $\mathbf{4}\boldsymbol{c}$ upstream from the blade section in the LRPM case. Thus, the stall onset cannot in this case obviously be attributed to the blade-vortex interaction.

In this region, the mechanisms at the origin of stall appear to be more difficult to analyze than in the inner part of the blade (region "A"). To get a better understanding of the correlation between the motion of the blade and the stall events, further analysis of the phenomena occurring at the tip region of the blade is necessary. The azimuthal evolution of the pitch angle, the Mach number, the torsion angle and the sectional pitching moment coefficient at the $\boldsymbol{r/R = 0.915}$ section are represented in Figures 18, *(a)*, *(b)* and *(c)* respectively for the HRPM, MRPM and LRPM cases. The chordwise flow-separation areas are also illustrated in grey in these figures (*bottom*) in order to compare the azimuthal phase of the phenomena. The chordwise position of the supersonic areas ($\boldsymbol{K_p - K_{p,crit} < 0}$, $\boldsymbol{K_{p,crit}}$ is the pressure coefficient corresponding to a sonic flow) at the considered section is also included in dashed line in the bottom of Figure 18 for the three test cases.

In order to quantify the effect of the tip vortex emitted by the previous blade on the angle of attack, the vertical component of the induced velocity $\boldsymbol{V_{iz}}$ has been extracted in the vicinity of the blade. The extraction was made one chord upstream the leading edge and at the same vertical level as the quarter chord point of the blade in order to avoid the perturbation induced by the blade itself. A parametric study has been performed (not shown) to select the extraction point. It allows to estimate at each time step the induced angle of attack seen by the blade section: $\boldsymbol{\alpha_i = arctan[V_{iz}/V_{blade}]}$ with

$V_{blade} = \Omega r + V_\infty sin(\psi) cos(\alpha_t)$. The induced angle of attack is illustrated at the $r/R = 0.915$ section in Figure 18 for the three cases too. The blade-vortex interaction is observed in these figures by the sudden variation and change of sign of the induced angle of attack around $\psi = 280\,\mathrm{deg}$.

In the MRPM case, the stall onset, at $\psi = 270\,\mathrm{deg}$, occurs when the blade is located in an area characterized by a maximum of the vertical component of the induced velocity due to the previous blade-tip vortex. It leads to a peak of the induced angle of attack $\alpha_i = 5\,\mathrm{deg}$ as observed in Figure 18, *(b)*. This high induced angle of attack is added to the high pitch angle observed on the blade at stall onset, which reaches $\theta = 17\,\mathrm{deg}$ at $\psi = 270\,\mathrm{deg}$ and leads to stall.

On the other hand, in the LRPM case, the pitch angle θ is found to be higher than for the two other cases (Figures 18, *a)* and *b)*). It reaches $\theta = 18\,\mathrm{deg}$ at the stall onset ($\psi = 260\,\mathrm{deg}$). Due to the tip vortex emitted by the previous blade which has not yet been met by the current blade, the blade is immersed in a flow with a positive upward vertical component of the induced velocity. In this case, the induced angle of attack is slightly higher than in the two other cases in this azimuthal region $\alpha_i = 4.2\,\mathrm{deg}$ at $\psi = 260\,\mathrm{deg}$. It is probably due to a lower velocity of the blade, V_{blade}. Indeed, as the thrust and the helicopter velocity is the same in all cases, the induced velocity V_{iz} is also roughly similar since it only depends on these two parameters according to the momentum theory in forward flight presented by Johnson in Ref. 44. Consequently, by the definition of the induced angle of attack, when the velocity of the blade V_{blade} is decreased, the induced angle of attack α_i is increased. Thus, it can be assumed that the variation of the angle of attack induced by the tip vortex could be high enough to trigger the stall in the LRPM case, even if the vortex is still located four chord lengths upstream of the blade in a constant radius cylindrical surface.

One can notice that in the HRPM case, the induced angle of attack is maximum and reaches $\alpha_i = 6\,\mathrm{deg}$ at $\psi = 280\,\mathrm{deg}$ as in the two other cases. However, in this case, the pitch angle of the blade is lower than in the other cases as $\theta = 15\,\mathrm{deg}$ at $\psi = 280\,\mathrm{deg}$. Consequently, it does not lead to stall.

To summarize, the pitch angle and the induced angle of attack obtained at the stall onset for each case are illustrated in Table 5. It is clear that if in all the cases, the behavior of the induced angle of attack is similar, the pitch angle differs. Consequently, the blade is more sensitive to angle of attack

variations in the LRPM case since the pitch angle is higher. Thus, the perturbation due to the vortex contributes more significantly to the stall onset in the LRPM case even when the vortex is still distant from the blade and $\alpha_{i,LRPM} < \alpha_{i,MRPM}$. When adding the pitch and induced angles, the highest values are obtained for this LRPM case, thus explaining why dynamic stall occurs before the actual blade-vortex interaction in this case.

Figure 18 also allows to highlight the link between the aerodynamics and the blade elastic response. The separation bubble bursts at $\psi = 280\,\mathrm{deg}$ for MRPM and at $\psi = 260\,\mathrm{deg}$ for LRPM leading to a strong negative pitching moment. This excites the blade torsion mode, as a local minimum of the torsion angle is reached directly after the stall event. For the HRPM (Figure 18, *a)*), the separation bubble does not burst and no stall is observed. Therefore, the amplitude of the blade torsion variation is smaller than for the lower RPM cases. The peak-to-peak torsion at stall is 0.3 deg for the HRPM and greater than 1.2 deg for the two other cases.

In region "B", the Mach number is, in all cases, close to 0.4 and a very small transonic region is seen. This transonic region disappears with the stall onset in the two lower RPM cases since the large flow-separation leads to a breakdown of the suction peak.

Analysis of Flow-Separation in Region "C"

The third flow-separation area, "C", located at the end of the fourth quadrant of the rotor disk, in Figures 12 and 13 concerns the blade-tip region. The flow-separation at $r/R = 0.915$, for $315\,\mathrm{deg} < \psi < 10\,\mathrm{deg}$ is also represented in Figures 18, *(a)*, *(b)* and *(c)*. At that azimuthal position, the pitch angle is still high ($\theta > 15\,\mathrm{deg}$). The blade undergoes a flapping down motion due to the Modane law which imposes $\beta_{1c} = \theta_{1s}$. Furthermore, the torsional deformation angle of the blade is at a local maximum of 1 to 1.5 deg. Thus, one can assume that both kinematic and deformation of the blade contribute to increase the angle of attack in region "C".

The process assumed through the rotormaps analysis of Figure 15 is very similar to the one observed in region "B". A small leading edge separation bubble is predicted for all cases at the end of the fourth quadrant which bursts at the blade-vortex interaction for the LRPM case. In Figure 17, the

isocontours of the Q-criterion for the blade at $\psi = 320\,\mathrm{deg}$ are presented for all the cases. This azimuthal position has been chosen to evaluate the influence of the rotor wake on stall at the blade-tip $r/R > 0.915$ in region "C" in Figures 7, 5 and 9. A second blade-vortex interaction takes place when the blade is at $\psi = 320\,\mathrm{deg}$. Indeed, in this azimuthal range, the blade encounters the tip vortex emitted by the blade half a revolution earlier interacting with the previous dynamic stall event of region "B", which was convected behind the rotor. The vorticity in the vortex impacted is higher in the LRPM case than in HRPM case by 30% (not shown). This high vorticity probably contributes to increase the vortex-induced angle of attack. Finally, the mechanisms triggering flow-separation in region "C" seem to be a combination of several phenomena. The blade-vortex interaction coupled with the positive torsion angle and the high pitch angle (Figures 18, *a)*, *b)* and *c)*) probably lead to this second stall event, observed in the sectional airloads of the LRPM case for $\psi = 330\,\mathrm{deg}$ (Figure 9, *c)*).

Analysis of Flow-Separation in Region "D"

Flow-separation "D" occurs in a high Mach number region with Mach number between 0.6 and 0.7. The evolution of the local Mach number and the torsion angle at $r/R = 0.915$ is presented in Figure 18, *a)* for the HRPM case, in Figure 18, *b)* for the MRPM case and in Figure 18, *c)* for the LRPM case.

A flow-separation is observed in this region for all cases. It occurs earlier with a high RPM because the shock wave appears earlier due to a high Mach number coupled with relatively high angles of attack. In region "D", the small separation bubbles of length close to 5 %c (HRPM) to 10 %c (LRPM) are observed at the root of the shock wave, defined as the recompression edge of supersonic regions.

Two lobes are observed in region "D" for the LRPM case (see Figure 12, *c)*). Each area also coincides perfectly with a positive torsion peak seen in Figure 18, *c)*. In the first event, the torsion adds 2 deg to the local angle of attack of the blade, which is significantly higher than for the two other RPM cases (Figures 18, *a)* and *b)*). It is observed that the stronger the stall is on the retreating blade,

the higher the torsion deformation amplitude is. Since the stall induces strong and impulsive pitching moments, one can think that it excites the torsion mode of the blade. This high torsion deformation can promote the flow-separation on the advancing blade.

Sectional normal forces and pitching moments do not show strong variations in these azimuthal and radial positions. Thus, flow-separation occuring in region "D" does not lead to stall in these three flight conditions.

However, variations of the pitching moment are observed notably in the LRPM case, where the separation bubble in region "D" is longer. A positive pitching moment is observed in the azimuthal region of the first lobe. It is probably due to the position of the separation bubble: $\mathbf{0.1} \leq \boldsymbol{x/c} \leq \mathbf{0.25}$.

Conclusion

Loose coupling simulations between the CFD code *elsA* and the CA code HOST have been carried out for three helicopter flight conditions undergoing dynamic stall. They correspond to the same flight condition of the helicopter at high speed and high thrust forward flight, with three different main rotor RPM regimes. This variation of RPM allows to go from a light to a deep stall condition. The main conclusions of this numerical analysis are as follows:

1. For all cases, the numerical simulations have shown satisfactory agreement with the experimental data with regard to trim parameters, airloads and structural loads. Dynamic stall events are correctly predicted in magnitude and phase.

2. Different stall events have been distinguished for each case. The stall intensity increases with the decrease in the RPM. A trailing edge stall is observed for all cases in the inner part of the blade. For the two highest RPM cases, the blade-tip undergoes one stall event at the beginning of the fourth quadrant of the rotor disk while it sees a double stall in the fourth quadrant for the lowest RPM case.

3. The mechanisms that lead to these different stall events have been investigated. The onset of stall has been associated with the impact of the tip vortex generated by the other blades. The

trailing edge stall and the strong leading edge stall occurring on the blade could be triggered by the angle of attack induced by the vortex passing close to the blade. Stall only occurs when the kinematic-induced angle of attack added to the vortex-induced angle of attack is high enough. The second stall event in the low RPM case seems connected to a second blade-vortex interaction. Further investigations will be necessary to determine the influence of the vortex features on the dynamic stall onset.

4. The torsional deformation of the blade is sensitive to stall events occurring on the rotor. The dynamic stall, generating periodic strong negative pitching moments, induces negative torsion angles. Thus, it excites the torsion mode and leads to positive torsion angle peaks in the first quadrant. It was shown that, for these flight conditions, these local torsion maxima are correlated to small flow-separations and, thus, to load variations.

Acknowledgments

Part of this research was supported by a DGA scholarship.
The studies presented in this article are making use of the elsA-ONERA software, whose co-owners are Airbus, Safran, and ONERA.

References

[1]McCroskey, W. J., "The Phenomenon of Dynamic Stall," NASA TM 81264, 1981.

[2]McCroskey, W. J., and, Fisher, R. K., "Detailed Aerodynamic Measurements on a Model Rotor in the Blade Stall Regime," *Journal of the American Helicopter Society*, Vol. 17, January 1972, pp. 2030, DOI:10.4050/jahs.17.1.20.

[3]McCroskey, W. J., and, McAlister, K. W., and, Carr, L. W., and, Pucci, S. L., "An Experimental Study of Dynamic Stall on Advanced Airfoil Sections," NASA TM 84245, 1982.

[4]Piziali, R. A., "2D and 3D Oscillating Wing Aerodynamics for a Range of Angles of Attack Including Stall," NASA TM 4632, 1994.

[5]Mulleners, K., and, Raffel, M., "The Onset of Dynamic Stall Revisited," *Experiments in Fluids*, Vol. 52, March 2012, pp. 779793, DOI:10.1007/s00348-011-1118-y.

[6]Mulleners, K., and, Raffel, M., "Dynamic Stall Development," *Experiments in Fluids*, Vol. 54, February 2013, DOI:10.1007/s00348-013-1469-7.

[7]Pailhas, G., and, Houdeville, R., and, Barricau, P., and, Le Pape, A., and, Faubert, A., and, Loiret, P., and, David, F., "Experimental Investigation of Dynamic Stall," Proceedings of the 31st European Rotorcraft Forum, Florence, Italy, 2005.

[8]Richter, K., and, Le Pape, A., and, Knopp, T., and, Costes, M., and, Gleize, V., and, Gardner, A. D., "Improved Two-Dimensional Dynamic Stall Prediction with Structured and Hybrid Numerical Methods," *Journal of the American Helicopter Society*, **56**, 042007 (2011), DOI:10.4050/JAHS.56.042007.

[9]Ekaterinaris, J. A., and, Platzer, M. F., "Computational Prediction of Airfoil Dynamic Stall," *Progress in Aerospace Sciences*, Vol. 33, April 1998, pp. 759 846, DOI:10.1016/S0376-0421(97)00012-2.

[10]Srinivasan, G. R., and, Ekaterinaris, J. A., and, McCroskey, W. J., "Evaluation of Turbulence Models for Unsteady Flows of an Oscillating Airfoil," *Computers & Fluids*, Vol. 24, September 1995, pp. 833 861, DOI:10.1016/0045-7930(95)00016-6.

[11]Costes, M., and, Gleize, V., and, Le Pape, A., and, Richez, F., "Numerical Investigation of Laminar/Turbulent Transition Effects on the Dynamic Stall of an Oscillating Airfoil," Proceedings of the American Helicopter Society 4th Decennial Specialists Conference on Aeromechanics, San Francisco, CA, 2008.

[12]Richter, K., and, Koch, S., and, Gardner, A. D., and, Mai, H., and, Klein, A., and, Rohardt, C. H., "Experimental Investigation of Unsteady Transition on a Pitching Rotor Blade Airfoil," *Journal of the American Helicopter Society*, **59**, 012001 (2014), pp. 112, DOI:10.4050/jahs.59.012001.

[13]Costes, M., and, Richez, F., and, Le Pape, A., and, Gavériaux, R., "Numerical Investigation of Three-Dimensional Effects during Dynamic Stall," Proceedings of the 37th European Rotorcraft Forum, Milan, Italy, 2011.

[14]Gardner, A. D., and, Klein, C., and, Sachs, W. E., and, Henne, U., and, Mai, H., and, Richter,

K., "Investigation of Three-Dimensional Dynamic Stall on an Airfoil using Fast-Response Pressure-Sensitive Paint," *Experiments in Fluids*, Vol. 55, August 2014, DOI:10.1007/s00348-014-1807-4.

[15]Le Pape, A., and, Pailhas, G., and, David, F., and, Deluc, J.-M., "Extensive Wind Tunnel Tests Measurements of Dynamic Stall Phenomenon for the OA209 Airfoil Including 3D Effects," Proceedings of the 33rd European Rotorcraft Forum, Kazan, Russia, 2007.

[16]Costes, M., and, Richez, F., and, Le Pape, A., and, Gavériaux, R., "Numerical Investigation of Three-Dimensional Effects during Dynamic Stall," *Aerospace Science and Technology*, Vol. 47, December 2015, pp. 216237, DOI:10.1016/j.ast.2015.09.025.

[17]Kaufmann, K., and, Costes, M., and, Richez, F., and, Gardner, A. D., and, Le Pape, A., "Numerical Investigation of Three-Dimensional Static and Dynamic Stall on a Finite Wing," *Journal of the American Helicopter Society*, **60**, 032004 (2015), DOI:10.4050/JAHS.60.032004.

[18]Jain, R., and, Le Pape, A., and, Grubb, A. L., and, Costes, M., and, Richez, F., and, Smith, M. J., "High-Resolution Computational Fluid Dynamics Predictions for the Static and Dynamic Stall of a Finite-Span OA209 Wing," *Journal of Fluids and Structures*, Vol. 78, April 2018, pp. 126 145, DOI:10.1016/j.jfluidstructs.2017.12.012.

[19]Kaufmann, K., and, Merz, C. B., and, Gardner, A. D., "Dynamic Stall Simulations on a Pitching Finite Wing," *Journal of Aircraft*, Vol. 54, July 2017, pp. 13031316, DOI:10.2514/1.C034020.

[20]Schwermer, T., and, Gardner, A. D., and, Raffel, M., "A Novel Experiment to Understand the Dynamic Stall Phenomenon in Rotor Axial Flight," *Journal of the American Helicopter Society*, **64**, 012004 (2019), DOI:10.4050/jahs.64.012004.

[21]Raghav, V., and, Komerath, N., "Dynamic Stall Life Cycle on a Rotating Blade in Steady Forward Flight," *Journal of the American Helicopter Society*, **60**, 032007 (2015), DOI:10.4050/jahs.60.032007.

[22]Gardner, A. D., and, Richter, K., "Influence of Rotation on Dynamic Stall," *Journal of the American Helicopter Society*, **58**, 032001 (2013), DOI:10.4050/jahs.58.032001.

[23]Letzgus, J., and, Keßler, M., and, Krämer, E., "CFD-Simulation of Three-Dimensional Dynamic Stall on a Rotor with Cyclic Pitch Control," Proceedings of the 41st European Rotorcraft Forum, Munich, Germany, 2015.

[24]Letzgus, J., and, Gardner, A. D., and, Schwermer, T., and, Keßler, M., and, Krämer, E., "Numer-

ical Investigations of Dynamic Stall on a Rotor with Cyclic Pitch Control," *Journal of the American Helicopter Society*, **64**, 012007 (2019), DOI:10.4050/jahs.64.012007.

[25]Bousman, W. G., "A Qualitative Examination of Dynamic Stall from Flight Test Data," *Journal of the American Helicopter Society*, Vol. 43, October 1998, pp. 279295.

[26]Kufeld, R. M., and, Balough, D. L., and, Cross, J. L., and, Studebaker, K. F., and, Jennison, C. D., and, Bousman, W. G., "Flight Testing the UH-60A Airloads Aircraft," Proceedings of the 50th American Helicopter Society International Annual Forum and Technology Display, Washington, DC, 1994.

[27]Mulleners, K., and, Kindler, K., and, Raffel, M., "Dynamic Stall on a Fully Equipped Helicopter Model," *Aerospace Science and Technology*, Vol. 19, June 2012, pp. 7276, DOI:10.1016/j.ast.2011.03.013.

[28]Potsdam, M., and, Yeo, H., and, Johnson, W., "Rotor Airloads Prediction Using Loose Aerodynamic/Structural Coupling," *Journal of Aircraft*, Vol. 43, May 2006, pp. 732742, DOI:10.2514/1.14006.

[29]Yeo, H., and, Potsdam, M., and, Ortun, B., and, Truong, K. V., "High-Fidelity Structural Loads Analysis of the ONERA 7A Rotor," *Journal of Aircraft*, Vol. 54, September 2017, pp. 18251839, DOI:10.2514/1.c034286.

[30]Ortun, B., and, Potsdam, M., and, Yeo, H., and, Truong, K. V., "Rotor Loads Prediction on the ONERA 7A Rotor Using Loose Fluid/Structure Coupling," *Journal of the American Helicopter Society*, **62**, 032005 (2017), DOI:10.4050/jahs.62.032005.

[31]Richez, F., "Numerical Analysis of Dynamic Stall for Different Helicopter Rotor Flight Conditions," Proceedings of the 73rd American Helicopter Society International Annual Forum and Technology Display, Fort Worth, TX, 2017.

[32]Grubb, A. L., and, Castells, C., and, Jain, R., and, Richez, F., and, Smith, M. J., "High Fidelity CFD Analyses of Dynamic Stall on a Four-Bladed Fully Articulated Rotor System," Proccedings of the 74th American Helicopter Society International Annual Forum and Technology Display, Phoenix, AZ, 2018.

[33]Chaderjian, N. M., "Navier-Stokes Simulation of UH-60A Rotor/Wake Interaction Using Adap-

tive Mesh Refinement," Proceedings of the 73rd American Helicopter Society International Annual Forum and Technology Display, Fort Worth, TX, 2017.

[34]Letzgus, J., and, Keßler, M., and, Krämer, E., "Simulation of dynamic stall on an elastic rotor in high-speed turn flight," *Journal of the American Helicopter Society*, **65**, 022002 (2020), DOI:10.4050/jahs.65.022002.

[35]Richez, F., "Analysis of Dynamic Stall Mechanisms in Helicopter Rotor Environment," *Journal of the American Helicopter Society*, **63**, 022006 (2018), DOI:10.4050/jahs.63.022006.

[36]Crozier, P., "Recent Improvements in Rotor Testing Capabilities in the ONERA S1MA Wind Tunnel," Proceedings of the 20th European Rotorcraft Forum, Amsterdam, Netherlands, 1994.

[37]Cambier, L., and, Heib, S., and, Plot, S., "The ONERA elsA CFD Software: Input from Research and Feedback from Industry," *Mechanics & Industry*, Vol. 14, no. 3, June 2013, pp. 159174, DOI:10.1051/meca/2013056.

[38]Benoit, C., and, Péron, S., and, Landier, S., "Cassiopee: A CFD Pre- and Post-Processing Tool," *Aerospace Science and Technology*, Vol. 45, September 2015, pp. 272283, DOI:10.1016/j.ast.2015.05.023.

[39]Kok, J. C., "Resolving the Dependence on Freestream Values for the k- Turbulence Model," *AIAA Journal*, Vol. 38, July 2000, pp. 12921295, DOI:10.2514/2.1101.

[40]Liggett, N. D., and, Smith, M. J., Temporal Convergence Criteria for Time-Accurate Viscous Simulations of Separated Flows," *Computers & Fluids*, Vol. 66, August 2012, pp. 140156, DOI:10.1016/j.compfluid.2012.06.010.

[41]Richez, F., and, Ortun, B., "Numerical Investigation of the Flow Separation on a Helicopter Rotor in Dynamic Stall Configuration," Proceedings of the 42nd European Rotorcraft Forum, Lille, France, 2017.

[42]Benoit, B., and, Dequin, A.-M., and, Kampa, K., and, Grünhagen, W., and, Basset, P.-M., and, Gimonet, B., "HOST, a General Helicopter Simulation Tool for Germany and France," Proceedings of the 56th American Helicopter Society International Annual Forum and Technology Display, Virginia Beach, VA, January 2000.

[43]Cliquet, J., and, Houdeville, R., and, Arnal, D., "Application of Laminar-Turbulent Transi-

tion Criteria in Navier-Stokes Computations," *AIAA Journal*, Vol. 46, May 2008, pp. 11821190, DOI:10.2514/1.30215.

[44]Johnson, W., *Rotorcraft Aeromechanics*, Cambridge University Press, 2009.

List of Figures

List of Tables

Fig. 1: 7A rotor mounted in ONERA Modane S1MA wind tunnel.

Table 1: Selected flight conditions

	Ω, rpm	M_{tip}	μ	C_L/σ	C_X/σ	α_t, deg	θ_0, deg	θ_{1c}, deg	θ_{1s}, deg
Low RPM (**LRPM**)	964	0.616	0.315	0.11	0.0049	-6.75	9.7	3.6	-4.4
Moderate RPM (**MRPM**)	1022	0.646	0.3	0.1	0.0046	-6.7	8.4	3.15	-3.5
High RPM (**HRPM**)	1063	0.676	0.288	0.09	0.0042	-6.45	7.2	2.5	-3.05

Table 2: Trim target

	C_L/σ	C_X/σ	β_{1c}, deg	β_{1s}, deg
Low RPM (**LRPM**)	0.11	0.0049	-θ_{1s}	0.
Moderate RPM (**MRPM**)	0.1	0.0046	-θ_{1s}	0.
High RPM (**HRPM**)	0.09	0.0042	-θ_{1s}	0.

Table 3: Mesh Specification

Blade mesh size	$\mathbf{5.7 \times 10^6}$
y^+	0.6
Boundary layer points	35-50
Chordwise points	313
Radial points	155
Normal points	61
Leading edge spacing	0.1%c
Finest cartesian grid spacing	**9.3**%c
Extent of the cartesian grid	**1**1R

Table 4: Trim control angles comparison for each flight case

	LRPM	MRPM	HRPM
Experiment: $\boldsymbol{\alpha_t}$, deg	-6.75	-6.7	-6.45
elsA/HOST: $\boldsymbol{\alpha_t}$, deg	-6.44	-6.4	-6.1
Experiment: $\boldsymbol{\theta_0}$, deg	9.7	8.4	7.2
elsA/HOST: $\boldsymbol{\theta_0}$, deg	9.7	8.6	7.2
Experiment: $\boldsymbol{\theta_{1c}}$, deg	3.6	3.15	2.5
elsA/HOST: $\boldsymbol{\theta_{1c}}$, deg	3.9	3.36	2.8
Experiment: $\boldsymbol{\theta_{1s}}$, deg	-4.4	-3.5	-3.05
elsA/HOST: $\boldsymbol{\theta_{1s}}$, deg	-4.4	-3.7	-3.01

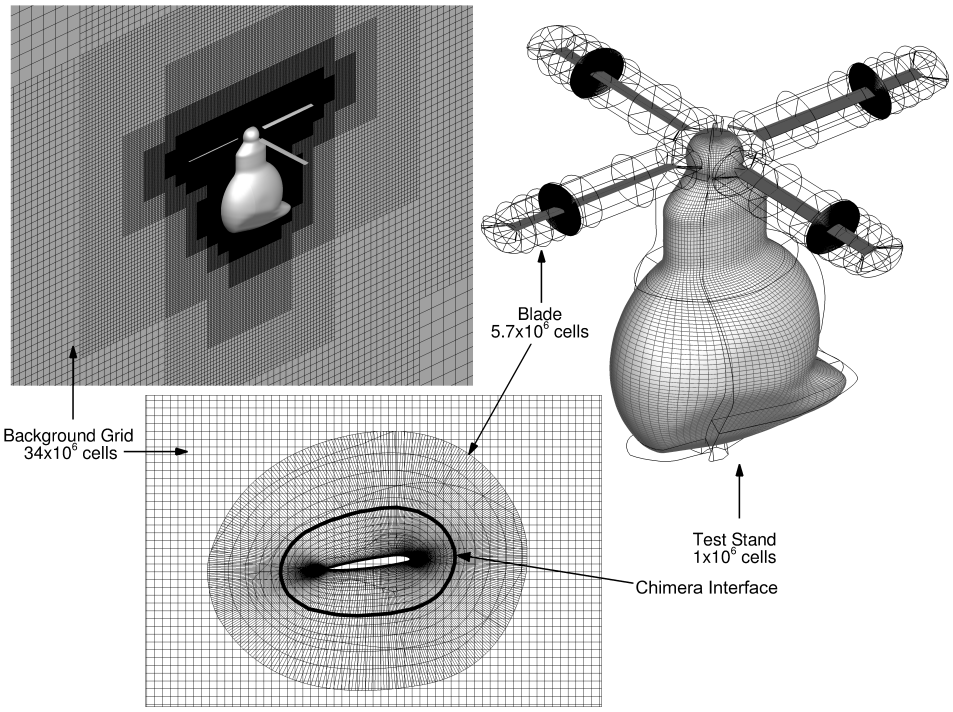

Fig. 2: Structured mesh: Chimera background grid, blades and test stand curvilinear grids.

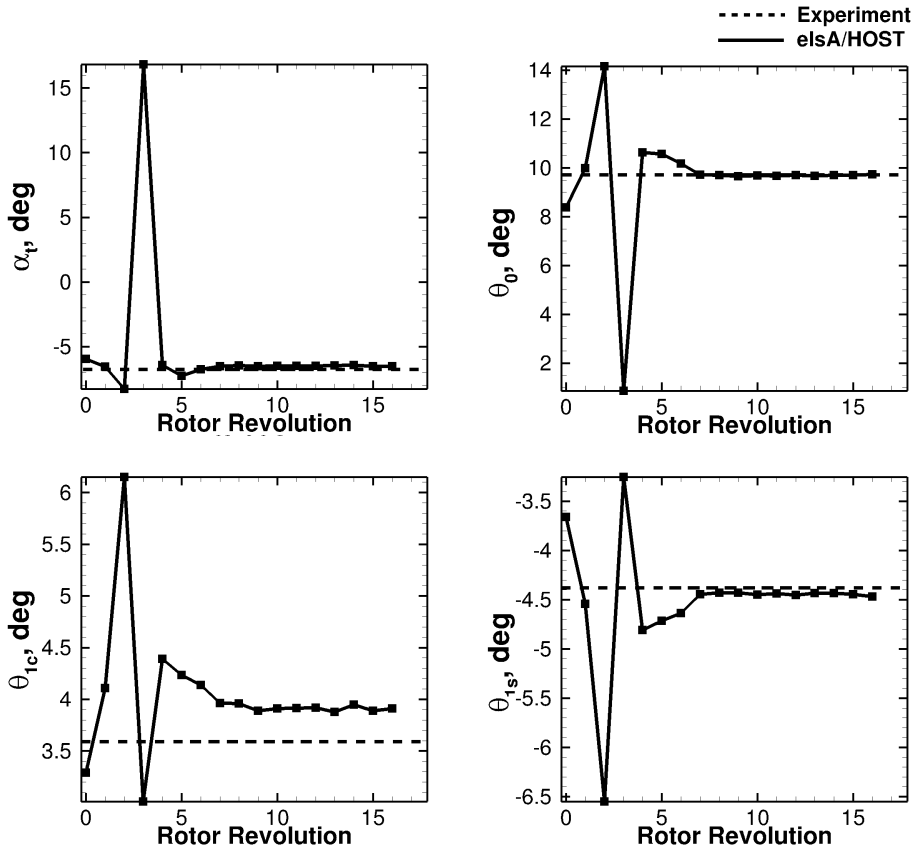

Fig. 3: Convergence of the control trim angles during the coupling process for the Low RPM case.

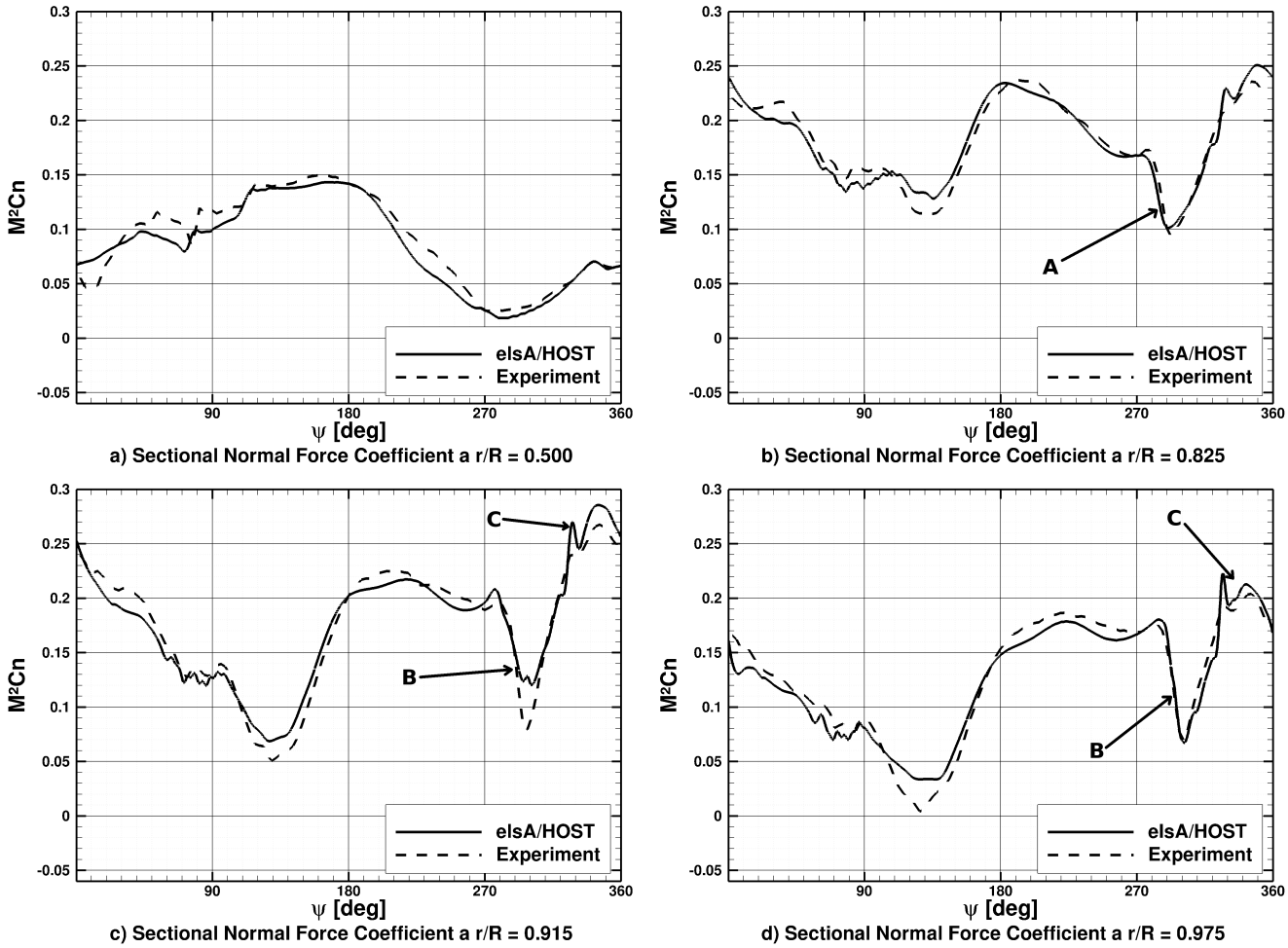

Fig. 4: Sectional normal force coefficient M^2C_n for the Moderate RPM case.

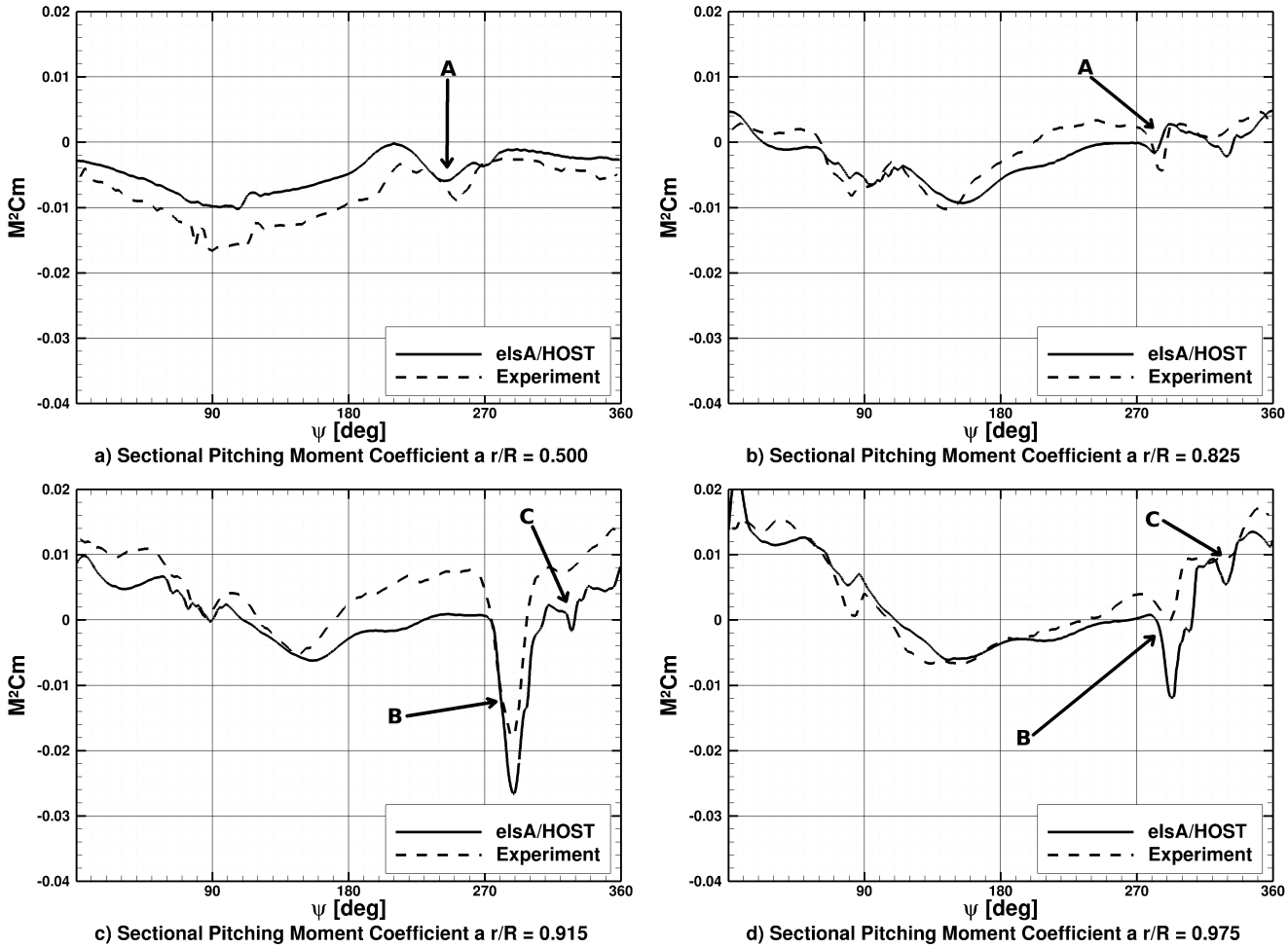

Fig. 5: Sectional pitching moment coefficient M^2C_m for the Moderate RPM case.

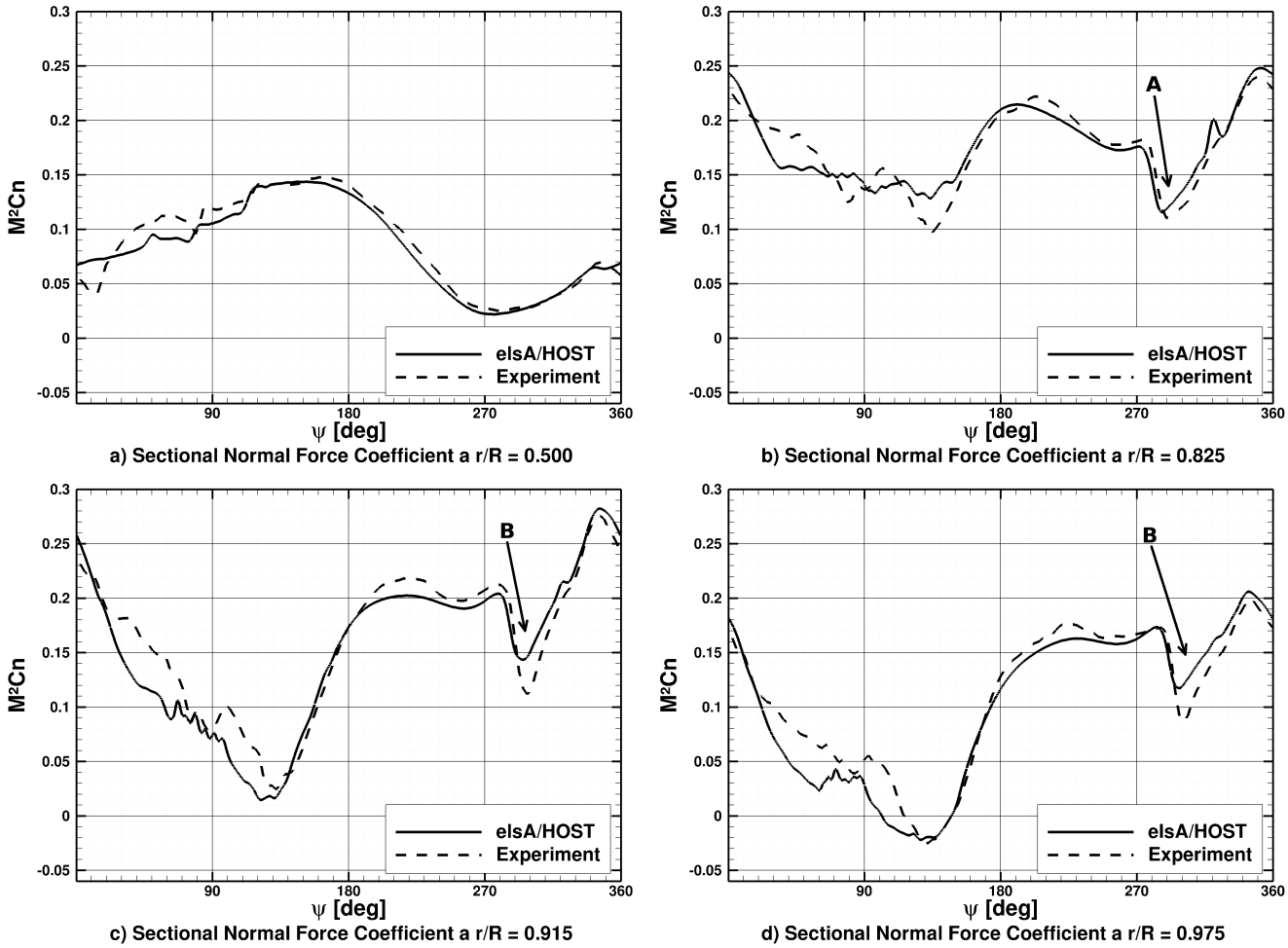

Fig. 6: Sectional normal force coefficient $\boldsymbol{M^2 C_n}$ for the High RPM case.

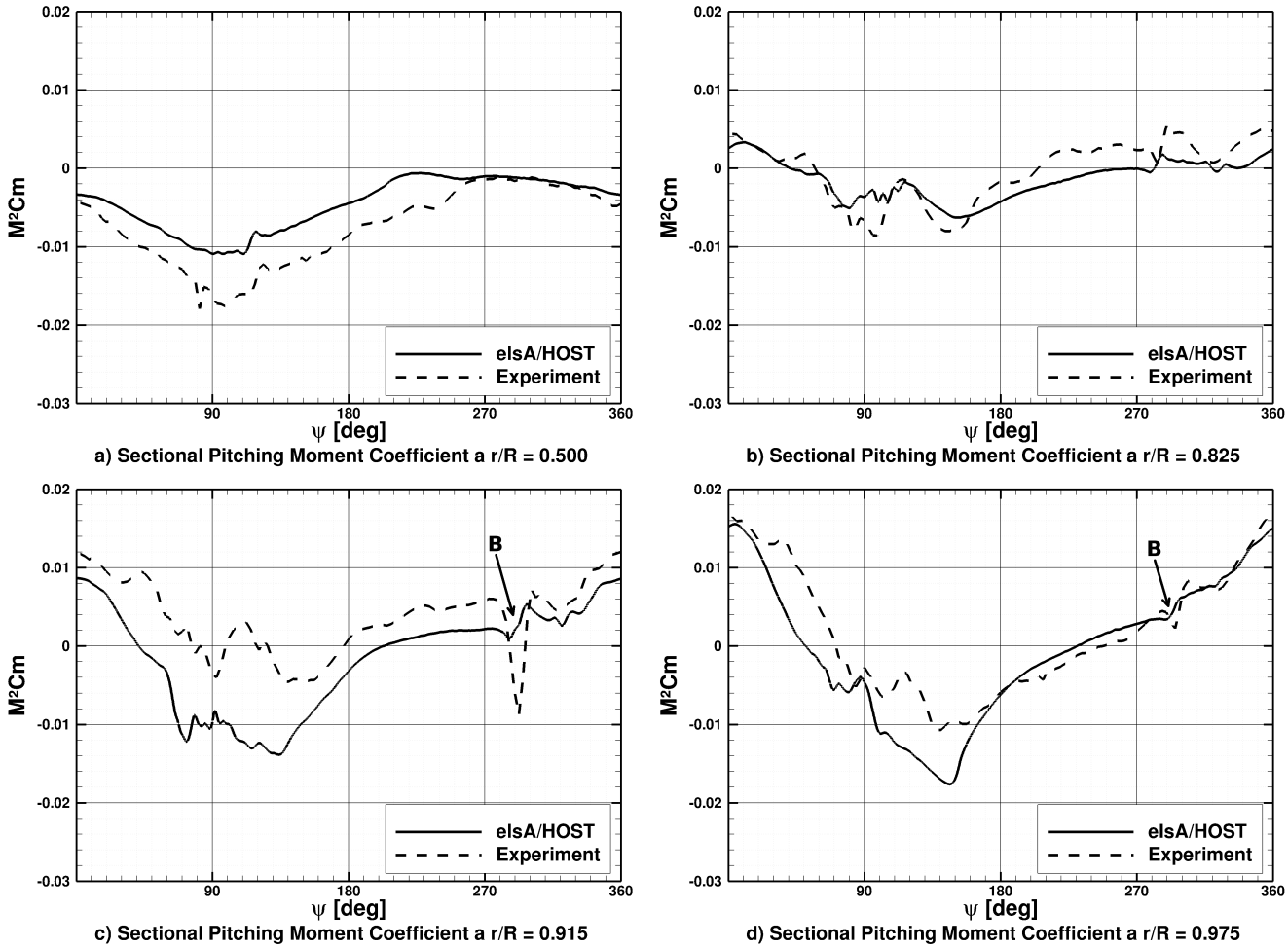

Fig. 7: Sectional pitching moment coefficient M^2C_m for the High RPM case.

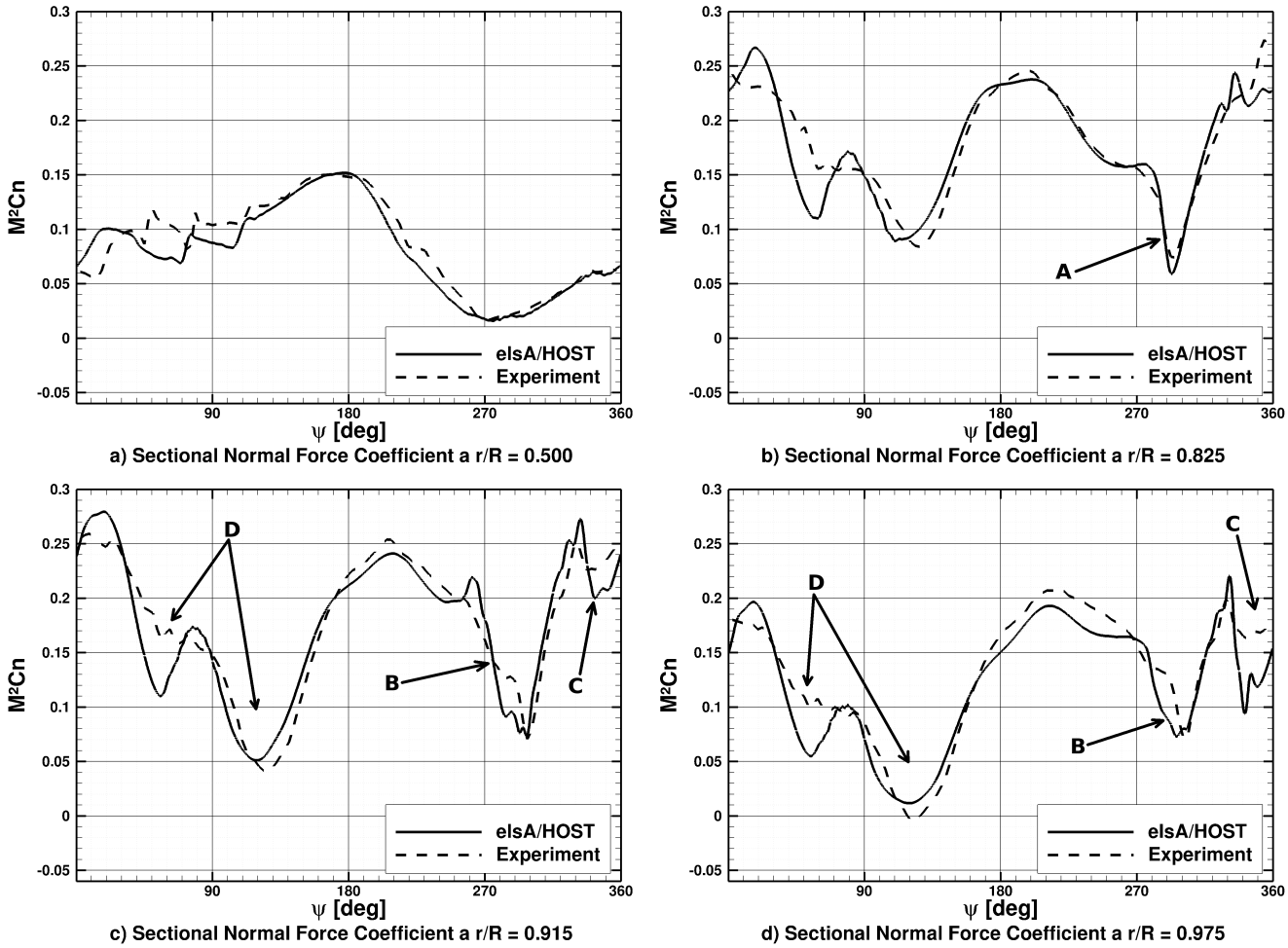

Fig. 8: Sectional normal force coefficient $\boldsymbol{M^2 C_n}$ for the Low RPM case.

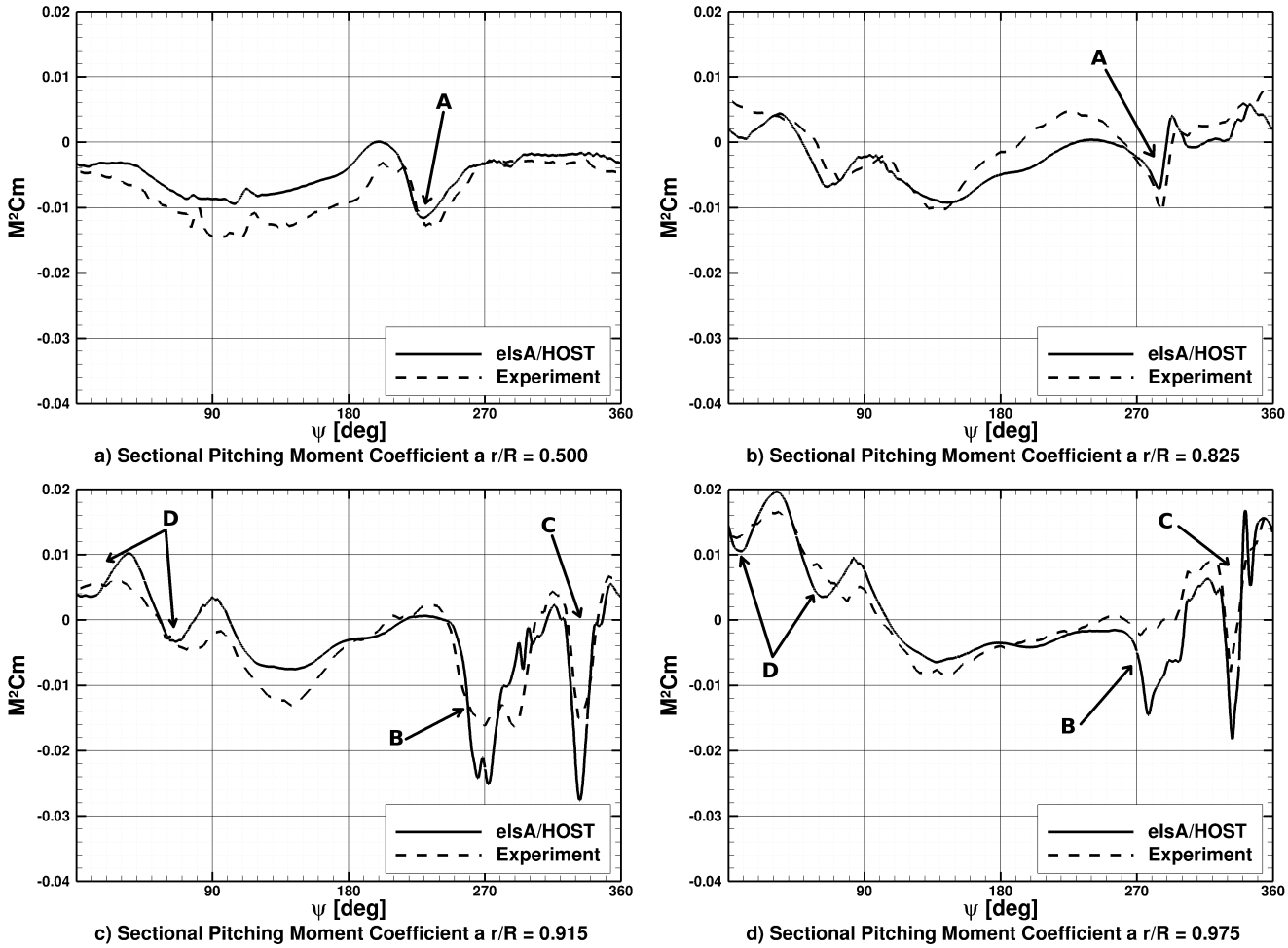

Fig. 9: Sectional pitching moment coefficient M^2C_m for the Low RPM case.

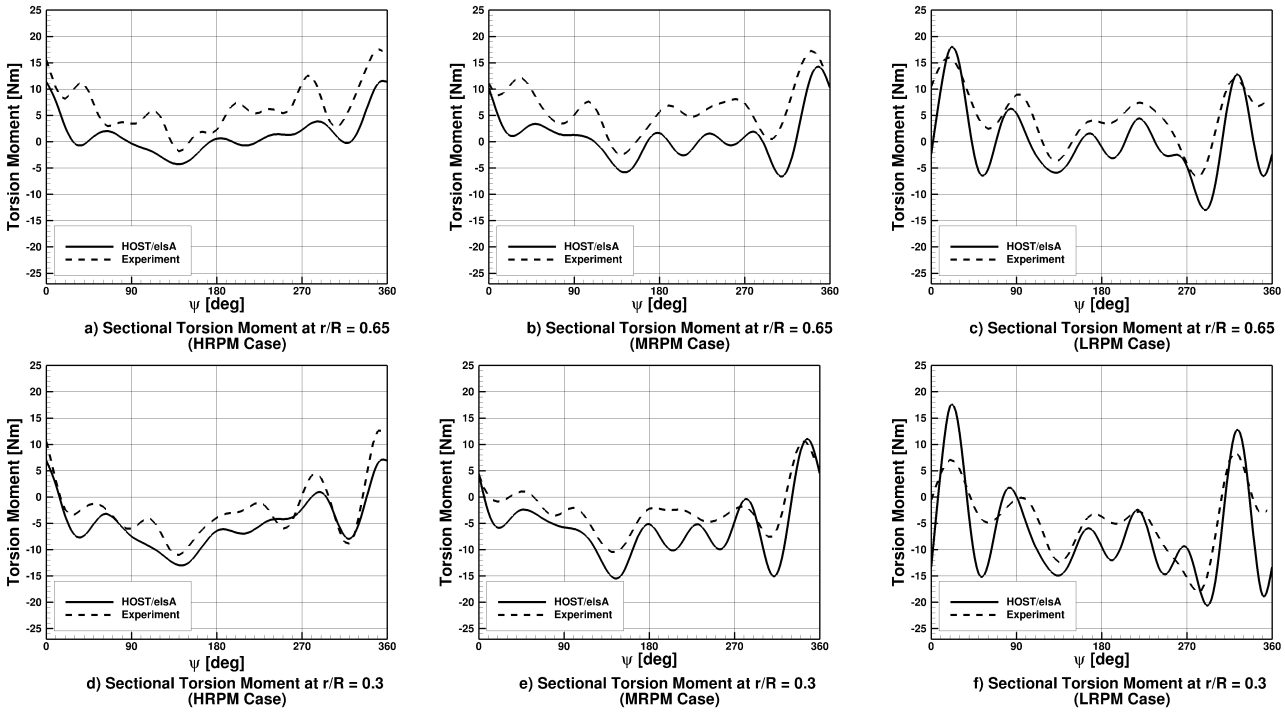

Fig. 10: Torsion moment.

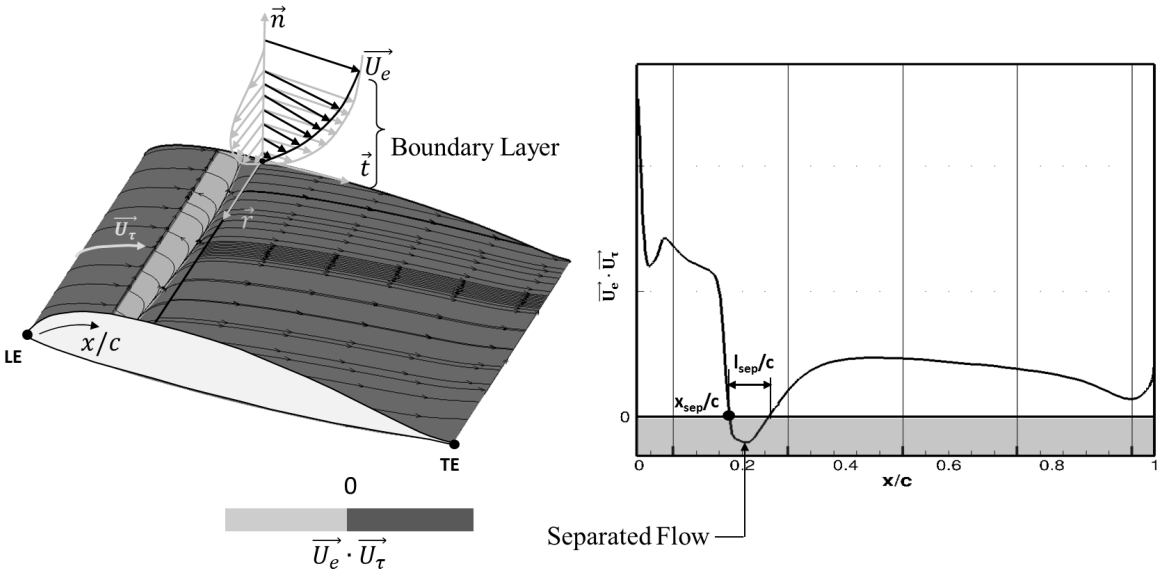

Fig. 11: Schematic representation of the method used for separated-flow detection.

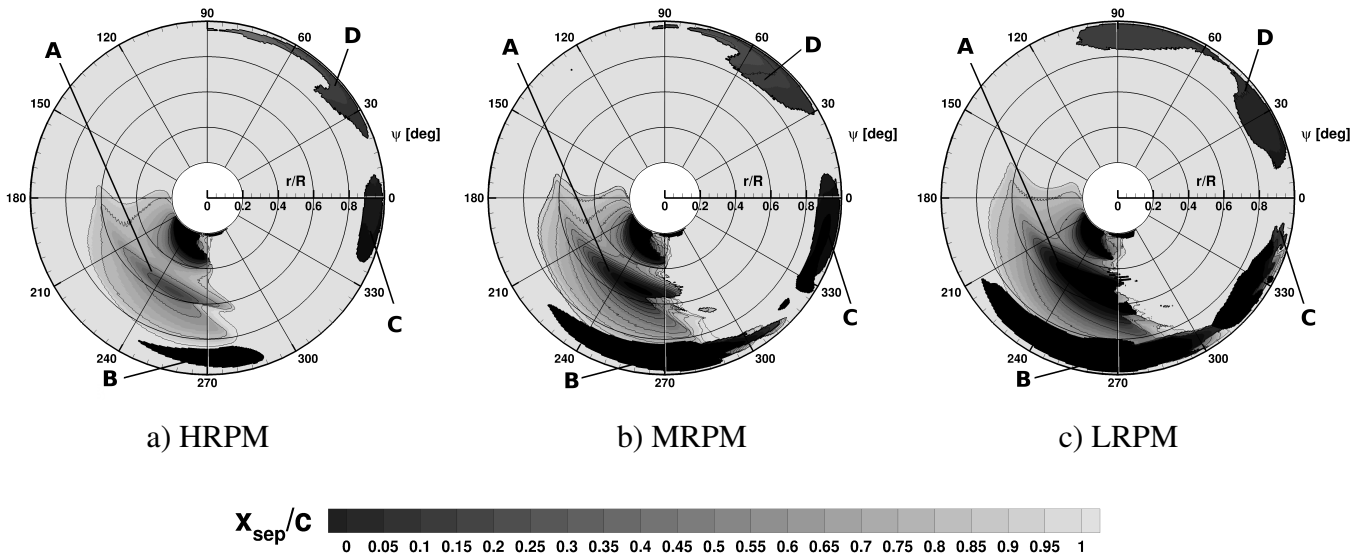

a) HRPM b) MRPM c) LRPM

Fig. 12: Rotormaps of the chordwise position of flow-separation $\boldsymbol{x_{sep}/c}$.

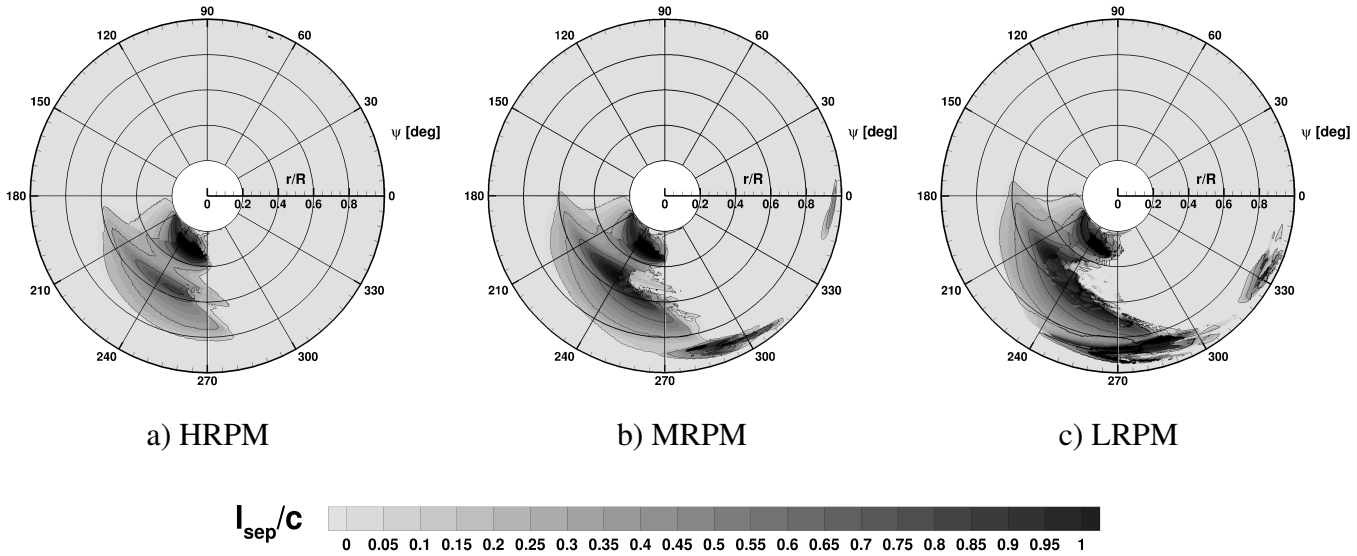

a) HRPM b) MRPM c) LRPM

Fig. 13: Rotormaps of the chordwise length of flow-separation l_{sep}/c.

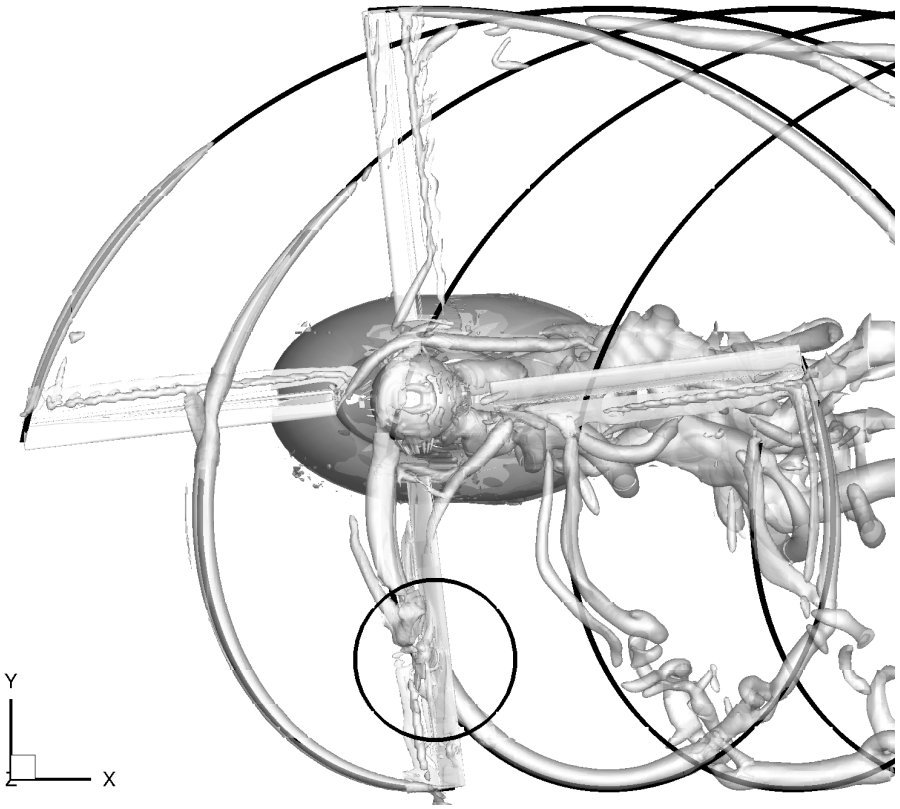

Fig. 14: Isocontour of Q-criterion for the blade at $\psi_{retreating\,blade} = 280\,\mathrm{deg}$. Black lines represent the analytical vortex lines.

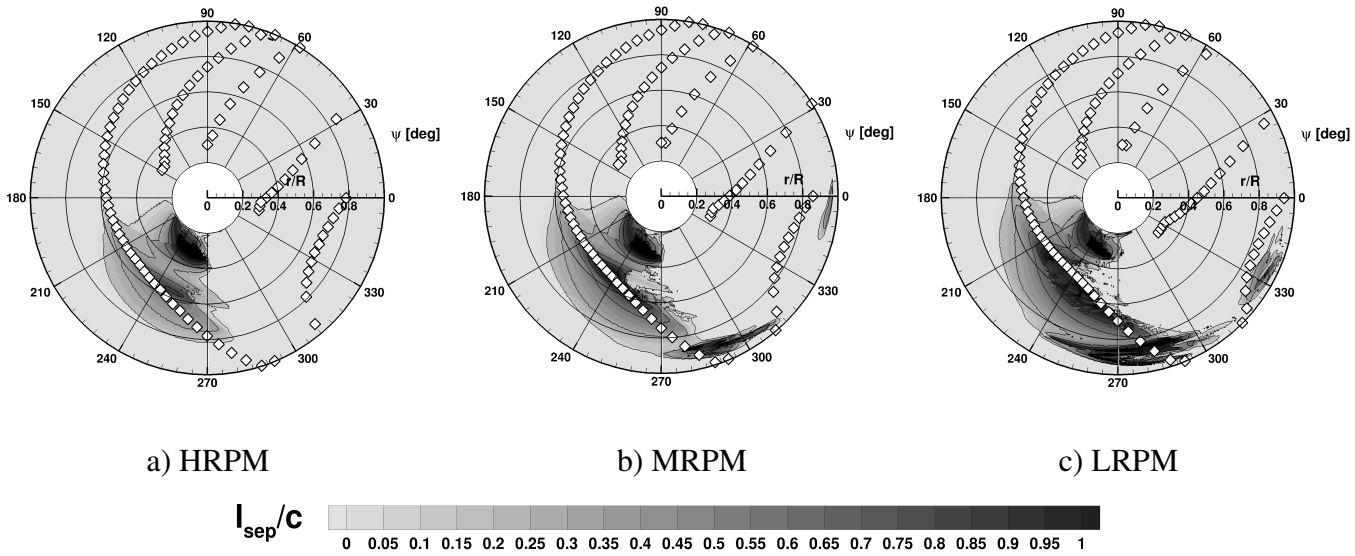

a) HRPM b) MRPM c) LRPM

Fig. 15: Rotormaps of the chordwise length of flow-separation l_{sep}/c (as Figure 13). ◇ symbols represent the analytical position of the blade-vortex interactions.

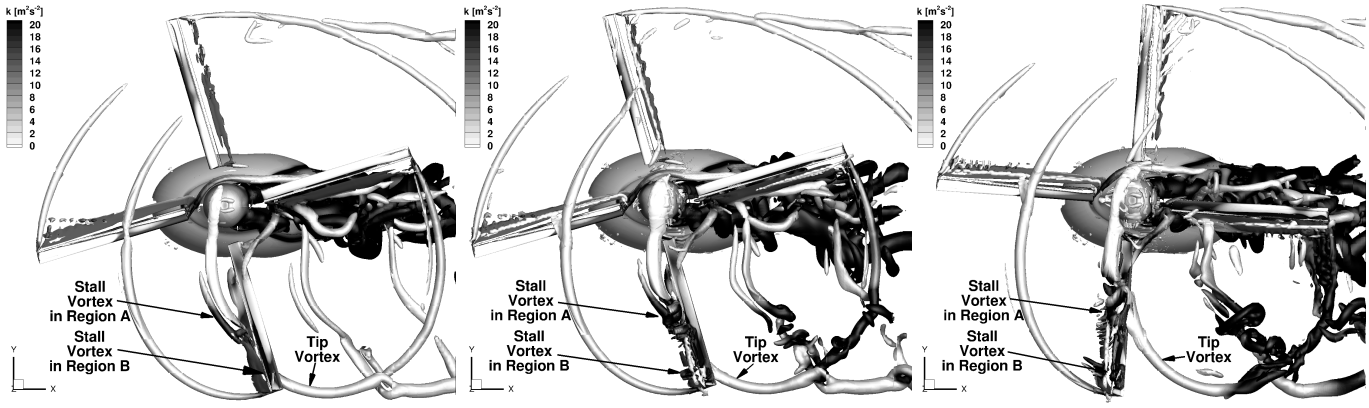

a) HRPM, $\psi_{retr.\,bl.} = 290\,\mathrm{deg}$ b) MRPM, $\psi_{retr.\,bl.} = 290\,\mathrm{deg}$ c) LRPM, $\psi_{retr.\,bl.} = 270\,\mathrm{deg}$

Fig. 16: Isocontour of Q-criterion colored by the turbulent kinetic energy for the blade at the azimuthal position of the minimum of $M^2 C_m$ associated to the event in flow-separation region "B".

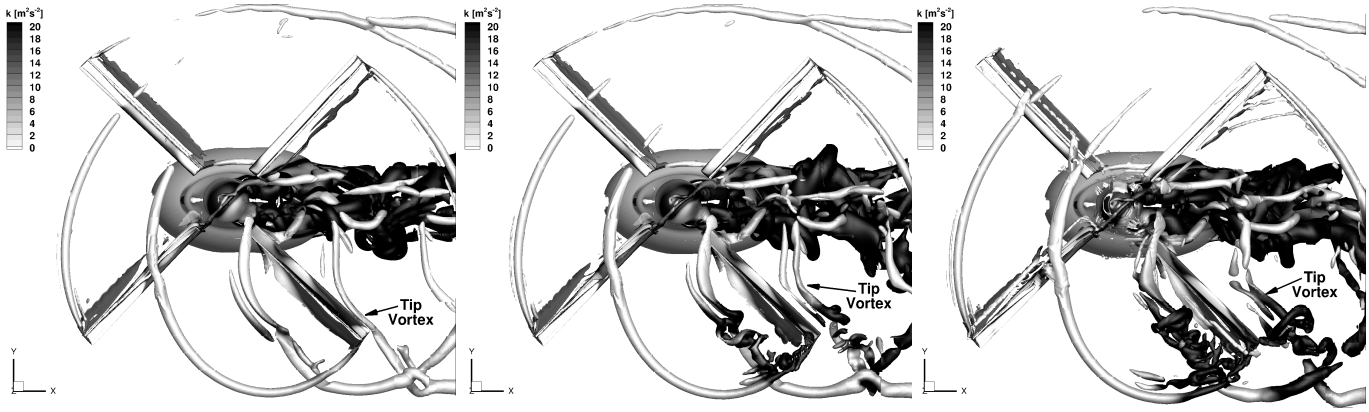

a) HRPM, $\psi_{retr.\,bl.} = 320\,\mathrm{deg}$ b) MRPM, $\psi_{retr.\,bl.} = 320\,\mathrm{deg}$ c) LRPM, $\psi_{retr.\,bl.} = 320\,\mathrm{deg}$

Fig. 17: Isocontour of Q-criterion colored by the turbulent kinetic energy for the blade at the azimuthal position of the minimum of $\boldsymbol{M^2 C_m}$ associated to the event in flow-separation region "C".

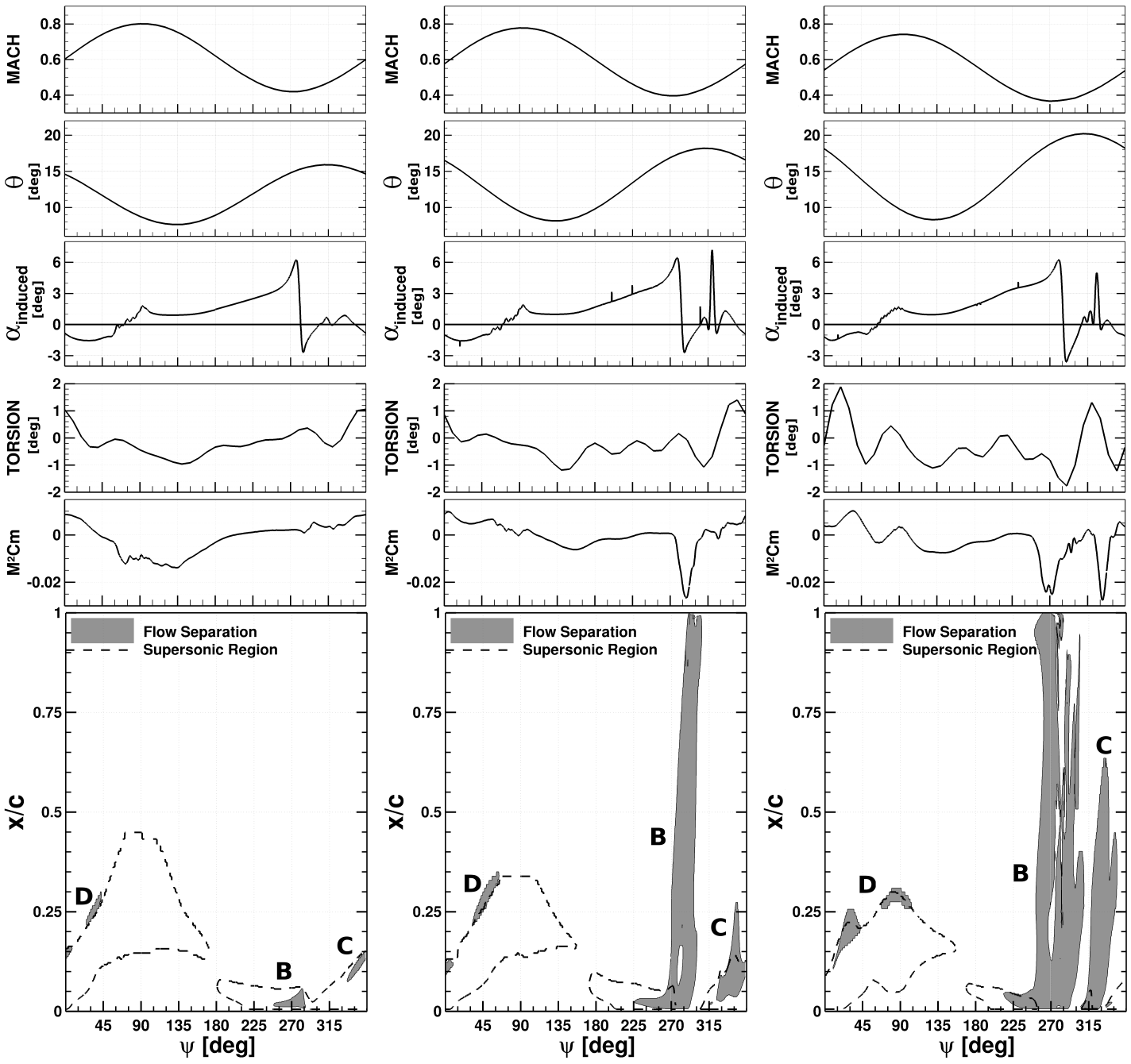

a) HRPM b) MRPM c) LRPM

Fig. 18: Representation of the evolution of the Mach number, torsion angle, the pitching moment coefficient, the flow-separation region and the chordwise position of the shock at $r/R = 0.915$ section.

Table 5: Quantification of the pitch angle and the induced angle of attack at stall

Case	psi [deg]	θ [deg]	α_i [deg]	$\theta + \alpha_i$ [deg]
Low RPM (**LRPM**)	260	18	4.2	22.2
Moderate RPM (**MRPM**)	270	17	5	22
High RPM (**HRPM**)	275	15	6	21